M A S T E R ' S T H E S I S

D I P L O M A R B E I T

Creep of shotcrete: Experiments and micromechanical modeling

Kriechverhalten von Spritzbeton: Experimentelle Untersuchungen und mikromechanische Modellierung

ausgeführt zum Zwecke der Erlangung des akademischen Grades eines Diplom-Ingenieurs

unter der Leitung von
Univ. Doz. Dipl.-Ing. Dr.techn. Roman Lackner
und
Dipl.-Ing. Dr.techn. Christian Pichler
E202
Institut für Mechanik der Werkstoffe und Strukturen
der Technischen Universität Wien

eingereicht an der Technischen Universität Wien
Fakultät für Bauingenieurwesen

von

Georg Handler
Matr.Nr.: 99 25 499
Beriningasse 7
A - 2700 Wiener Neustadt

Wien, im Jänner 2009

Mein herzlicher Dank gilt...

CHRISTIAN PICHLER für die Betreuung während der Erstellung dieser Arbeit,

ROMAN LACKNER für die Durchsicht derselben,

JOSEF EBERHARDSTEINER für die motivierende Wirkung auf die Menschen seines Umfelds,

KLAUS MEINHARD, der mir die Daten aus den Calorimeterversuchen zur Verfügung stellte und mir deren Auswertung erläuterte,

MATTHIAS ZEIML und ELISABETH AIGNER für das freundliche Miteinander im Büro,

DOMINIK DEJMEK, der mir stets weiterhalf, wenn der Server dies nicht mehr tat,

meinen Eltern und meinem Bruder, für ihre Liebe und die gelebte Geduld, und all den Freunden, Verwandten und besonderen Menschen, die mich vervollständigen.

Kurzfassung

Die realistische Beschreibung des Kriechverhaltens von jungem Spritzbeton ist für die Bestimmung des Auslastungsgrades von Spritzbetonschalen im Rahmen von Tunnelbauprojekten von entscheidender Bedeutung. In den letzten Jahren ermöglichten neuartige experimentelle Methoden sowie Fortschritte im Bereich der Materialmechanik die Entwicklung sogenannter Mehrskalenmodelle, die eine Beschreibung der für das Kriechverhalten von zementgebundenen Werkstoffen verantwortlichen physikalischen und chemischen Prozesse auf der Beobachtungsebene erlauben, auf der diese Prozesse tatsächlich wirksam sind. Das in [16] vorgeschlagene Mehrskalenmodell bildet die Grundlage der vorliegenden Arbeit, welche folgende Themen umfasst:

- *Homogenisierung des elastischen und viskoelastischen Materialverhaltens*

  Die Bestimmung der makroskopischen Eigenschaften erfolgt ausgehend von der sogenannten Mörtelebene (Aggregat in Zementsteinmatrix) unter Anwendung (i) der Kontinuumsmikromechanik (Mori-Tanaka Schema) und (ii) der Methode der finiten Elemente. Die Ergebnisse der beiden Homogenisierungsmethoden werden einander gegenübergestellt.

- *Kriechexperimente*

  Fünf verschiedene Spritzbetonmischungen, welche im Tunnelbauprojekt "Lainzer Tunnel" eingesetzt wurden, werden hinsichtlich ihres Kriechverhaltens untersucht. Die dadurch erhaltenen Kriechnachgiebigkeiten werden in Abhängigkeit des Hydrationsgrades dargestellt.

Schließlich erfolgt ein Vergleich der experimentellen Ergebnisse mit den Kriecheigenschaften, die mit dem Mehrskalenmodell prognostiziert wurden.

Abstract

The realistic description of the creep behavior of early-age shotcrete is essential for determination of the degree of loading of shotcrete linings serving as primary support in tunnel construction. In recent years, novel experimental methods and progress in the field of micromechanics have led to the development of so-called multiscale models, allowing the consideration of physical/chemical processes causing creep of early-age cement-based materials at the scale of their occurrence. This thesis departs from the multiscale model outlined in [16] and comprises:

- *Upscaling of elastic and viscoelastic material behavior*

  The macroscopic properties of shotcrete are determined by considering two material phases (cement paste and aggregate) at the so-called mortar-scale using (i) micromechanical methods (Mori-Tanaka scheme) and (ii) the Finite Element approach. The results obtained from the two upscaling methods are compared.

- *Creep experiments*

  Five different shotcrete mixtures, which have been employed in different sections of the tunnel construction project "Lainzer Tunnel", are investigated experimentally as regards their creep behavior. The obtained model parameters describing the creep behavior are determined as a function of the hydration degree.

Finally, the experimentally-obtained results are compared with those predicted by the multiscale model.

Contents

Chapter 1

Motivation

The increasing traffic of the continuously enlarging European Union requires the construction of new and the improvement of existing traffic infrastructure. Hereby, subterranean solutions are chosen in many cases. Therefore, the engineering field of tunnel construction will even become more important in the near future [15].

For the construction of tunnels according to the New Austrian Tunneling Method (NATM), the mechanical behaviour of its primary support, i.e, the shotcrete lining, is essential for the engineering and economic success of the tunnel project. In this context, the creep mechanisms present especially in early-age shotcrete strongly influence the loading of the shotcrete lining and, thus, the safety of the tunneling process. Recently, multiscale models for early-age cement-based materials were developed, correlating macroscopic material behavior of cement-based materials, such as creep, to physical/chemical processes occurring at finer scales of observation.

The multiscale model proposed in [16] provides the starting point for this thesis and is briefly reviewed in Appendix A. In Chapter 2, macroscopic properties of shotcrete are determined by considering a two-phase material (cement paste and aggregate), employing two upscaling methods based on continuum micromechanics and the finite element method, respectively (see also Appendices B to E). Finally, in Chapter 3, creep experiments for five different types of shotcrete (Appendix G) are presented and compared with the respective material response predicted by the multiscale model.

Chapter 2

Multiscale modeling of shotcrete

Multiscale models describe the complex material behavior considering information from different scales of observation. At each scale, the material is characterized by identifying homogeneous material phases as well as their spatial variation. Depending on the characteristics of the spatial variation, two different groups of modeling approaches can be distinguished (see [18]):

- Models based on studying discrete microstructures, which include e.g. (i) Periodic Microfield Approaches or Unit Cell Methods [1, 19, 12], (ii) Embedded Cell Approaches [4, 24, 20], and (iii) Windowing Approaches [9].
- Models based on statistical information of the inhomogeneous material, such as (i) Mean Field Approaches (MFA) [21] and (ii) Variational Bounding Methods.

According to [16], MFA may be used to model cement-based materials such as shotcrete, introducing three additional scales of observations below macroscale (see Figure 2.1):

- At the *mortar scale*, concrete is treated as a two-phase composite material consisting of a cement-paste matrix with aggregate inclusions.
- The *cement-paste scale* allows to split the cement-paste into different phases consisting of anhydrous cement, water, and hydration products.
- Low density (LD) and high density (HD) C-S-H are distinguished at the lowest scale of observation.

In Appendix A.1, the particular scales are described in detail. Appendix A.2 contains the hydration model used for determination of the volume fractions of the phases of early-age cement paste.

2.1 Upscaling of elastic properties

For determination of the macroscopic elastic properties of shotcrete, the two material phases (cement paste and aggregate) at mortar scale (Scale III) are considered within (i) the Mori-Tanaka scheme (MT) and (ii) a Finite Element (FE) approach.

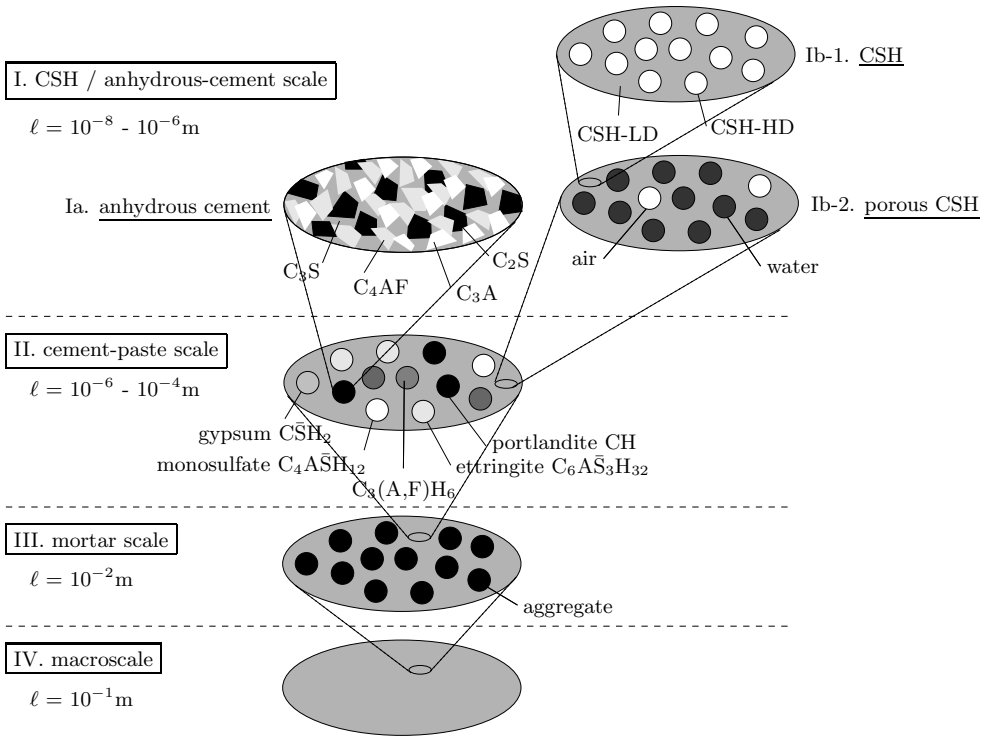

Figure 2.1: Scales of observation for cement-based materials [16] [l=size of representative volume element (RVE)]

In the FE model, plane-strain elements are used to discretize the RVE (Figure 2.2). During the numerical simulation, the nodes of the top boundary of the RVE exhibit similar vertical displacement, with the external force applied at the top, left node. For the left boundary, all horizontal displacements are locked and for the bottom boundary all vertical displamecements are restrained. Whereas Young's modulus in the out-of-plane direction is obtained from

$$E_z = f_a E_a + (1 - f_a) E_m, \tag{2.1}$$

where f_a, E_a, and E_m denote the aggregate volume fraction, Young's modulus of the aggregate and the matrix, respectively, $E_{x,y}$ and ν_{xy} are obtained from Hooke's law (see Appendix D) for plane strain, giving

$$E_{x,y} = \frac{E_z(\sigma_{xx}^3 + \sigma_{xx}^2\sigma_{yy} - \sigma_{xx}\sigma_{yy}^2 - \sigma_{yy}^3)}{\sigma_{xx}\sigma_{zz}^2 + \sigma_{xx}\sigma_{yy}\varepsilon_{xx}E_z + \sigma_{xx}^2\varepsilon_{xx}E_z - \sigma_{yy}\sigma_{zz}^2 - \sigma_{yy}^2\varepsilon_{yy}E_z - \sigma_{xx}\sigma_{yy}\varepsilon_{yy}E_z} \tag{2.2}$$

$$\nu_{xy} = \frac{-\sigma_{xx}^2\varepsilon_{yy}E_z - \sigma_{xx}\sigma_{yy}\varepsilon_{yy}E_z - \sigma_{xx}\sigma_{zz}^2 + \sigma_{xx}\sigma_{yy}\varepsilon_{xx}E_z + \sigma_{yy}^2\varepsilon_{xx}E_z + \sigma_{yy}\sigma_{zz}^2}{\sigma_{xx}\sigma_{zz}^2 + \sigma_{xx}\sigma_{yy}\varepsilon_{xx}E_z + \sigma_{xx}^2\varepsilon_{xx}E_z - \sigma_{yy}\sigma_{zz}^2 - \sigma_{yy}^2\varepsilon_{yy}E_z - \sigma_{xx}\sigma_{yy}\varepsilon_{yy}E_z}, \tag{2.3}$$

where $\sigma_{\alpha\alpha}$ and $\varepsilon_{\alpha\alpha}$ are the macroscopic stress and strain component. Figure 2.3 shows a comparison of the effective Young's moduli determined by the MT scheme and the FE calculation. The employed material parameters are listed in Table 2.1.

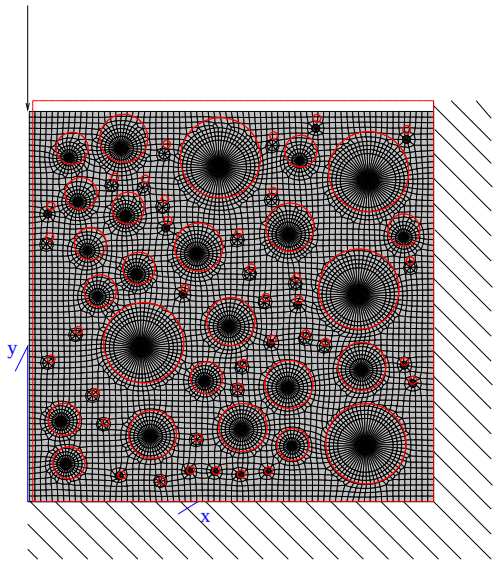

Figure 2.2: Boundary conditions (deformed shape)

	Poisson's ratio [–]	Young's modulus [GPa]
matrix	0.24	30
aggregate	0.24	50

Table 2.1: Elastic properties of material phases

2.2 Upscaling of viscous properties

For the upscaling of viscous material properties, the Maxwell model and a three-parameter model are used to describe the creep behavior of the matrix material (index "m"). The respective creep-compliance functions read:

$$J_m^{dev}(t) = \frac{1}{\mu_{m0}} + \frac{t}{\eta} \text{ (Maxwell model)} \tag{2.4}$$

and

$$J_m^{dev}(t) = \frac{1}{\mu_{m0}} + \frac{t}{\mu_v}\left(1 - e^{-\frac{\mu_v t}{\eta}}\right) \text{ (three-parameter model)}, \tag{2.5}$$

where μ_{m0} is the elastic shear modulus of the matrix. The viscosity η and the parameter μ_v describe the deviatoric creep behavior.

Considering the characteristics of the microstructure at mortar scale, Equations (2.6) to (2.10) [22] in Table 2.2 give access to the effective parameters μ_{eff} and k_{eff}, representing shear and bulk modulus of the homogenized material at macroscale. At the mortar scale,

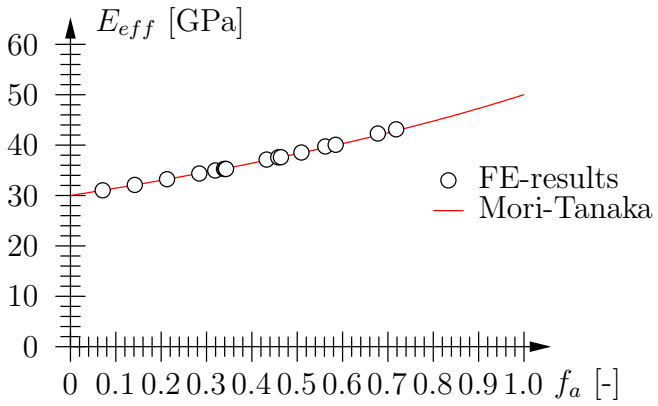

Figure 2.3: Effective Young's modulus determined from MT scheme and finite element model

shotcrete is characterized by the volume fraction f_a of the aggregate, the shear moduli μ_a and μ_m and the bulk moduli k_a and k_m of the aggregate and the cement-paste matrix, respectively. The two creep laws introduced in the previous subsection are considered in the homogenization formulas given in Table 2.2, employing the correspondence principle outlined in Appendix B.2. The effective creep behavior obtained from application of the correspondence principle is given in Appendix F.

The employed FE meshes and the boundary conditions were taken from Subsection 2.1. For comparison with the effective creep properties obtained from continuums micromechanics, the deviatoric creep compliance J_{eff}^{dev} and the volumetric creep compliance J_{eff}^{vol} are determined as:

$$J_{eff}^{dev}(t) = \frac{2(1+\nu_{xy})}{E_{x,y}} \quad \text{and} \quad J_{eff}^{vol}(t) = \frac{\varepsilon^{vol}}{\sigma^m} = \frac{\varepsilon_{xx}+\varepsilon_{yy}+\varepsilon_{zz}}{\frac{\sigma_{xx}+\sigma_{yy}+\sigma_{zz}}{3}} \tag{2.11}$$

Hereby, the definitions for $E_{x,y}$ and ν_{xy} can be found in Subsection 2.1. ε^{vol} and σ^m are the effective volumetric strain and mean value of the normal stresses, repectively. The material parameters used for the calculations are listed in Table 2.3. The given values for μ_a and k_a are used only for the FE calculation. For the continuum micromechanics approach, $\mu_a = k_a = 0$. Figures 2.4 and 2.5 depict the results of the comparison between the analytical and the numerical calculations.

As regards the analytical calculations, homogenization schemes for cylindrical inclusions are used.

The comparison reveals that the performance of the FE approach is very good and compares well to the MT results in case of a small amount of aggregate. For increasing amount of aggregate, the MT scheme -being restricted to dilute aggregate distributions- overestimates the effective creep compliance.

① unidirectional cylindrical elastic inclusions of high stiffness

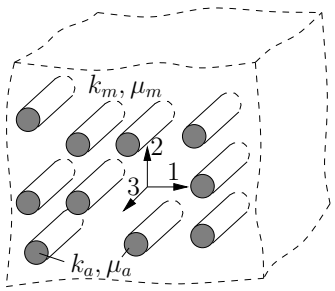

$$\mu_{12,eff} = \mu_m + f_a \frac{\mu_a - \mu_m}{1 + (1 - f_a)\frac{\mu_a - \mu_m}{\mu_p}} \tag{2.6}$$

$$k_{eff} = k_m + f_a \frac{k_a - k_m}{1 + (1 - f_a)\frac{k_a - k_m}{k_p}} \tag{2.7}$$

$$\text{with} \quad k_p = k_m + \mu_m \quad \text{and} \quad \mu_p = 2\mu_m \frac{k_m + \mu_m}{k_m + 2\mu_m} \tag{2.8}$$

② unidirectional cylindrical pores

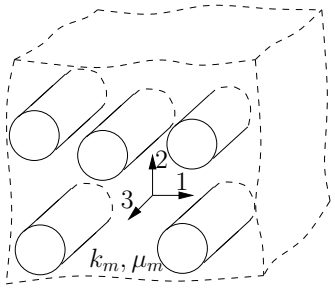

$$\mu_{12,eff} = \mu_m - \frac{f_p \mu_m}{1 - \frac{(1 - f_p)(\eta p + \mu_m)(k_m + 2\mu_m)}{2\eta p (k_m + \mu_m)}} \tag{2.9}$$

$$k_{eff} = k_m - \frac{f_p k_m}{1 - \frac{(1-f_p)k_m}{k_m + \mu_m}} \tag{2.10}$$

Table 2.2: Effective elastic parameters for different types of inclusions [22]

	inclusions of high stiffness (case ①)	pores (case ②)
μ_m[MPa]	120	12000
μ_a[MPa]	$1.2 \cdot 10^6$	$4.0 \cdot 10^{-9}$
k_m[MPa]	200	20000
k_a[MPa]	$2.0 \cdot 10^6$	$6.\dot{6} \cdot 10^{-9}$
η[MPa· s]	$3.0 \cdot 10^5$	$3.0 \cdot 10^7$
μ_v[MPa]	120	12000

Table 2.3: Material parameters used for upscaling of viscoelastic properties

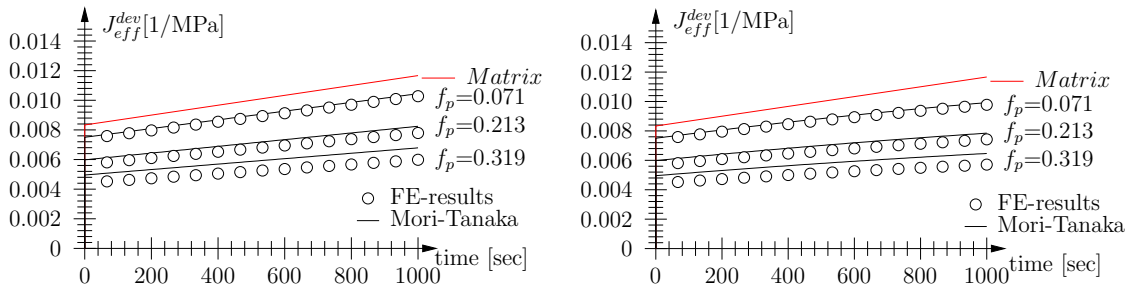

J^{dev}_{eff} for Maxwell model

J^{dev}_{eff} for three-parameter model

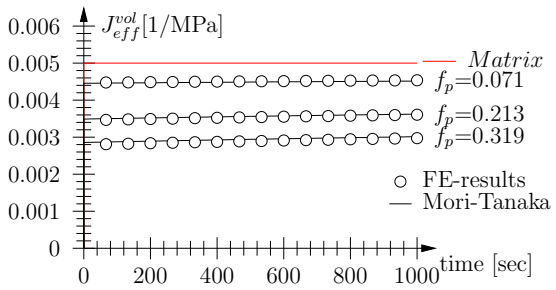

J^{vol}_{eff} for Maxwell model

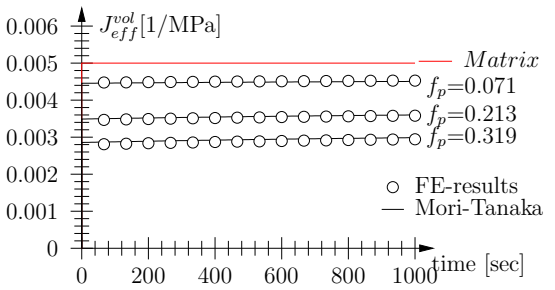

J^{vol}_{eff} for three-parameter model

Figure 2.4: Comparison of the results obtained by FE and MT calculation for case ① [according to Table 2.2]

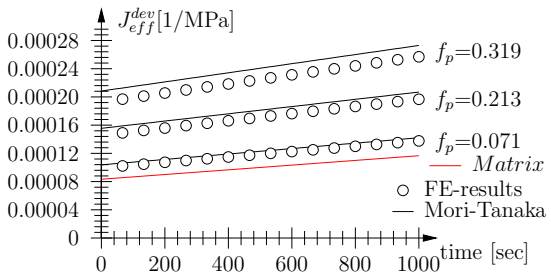

J^{dev}_{eff} for Maxwell model

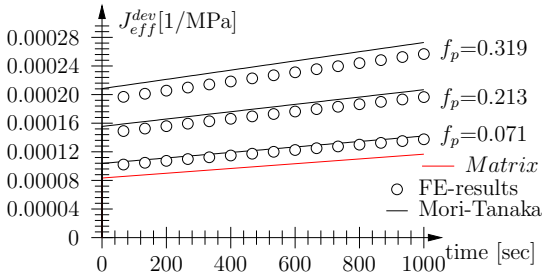

J^{dev}_{eff} for three-parameter model

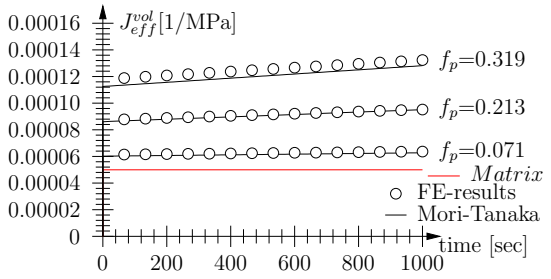

J^{vol}_{eff} for Maxwell model

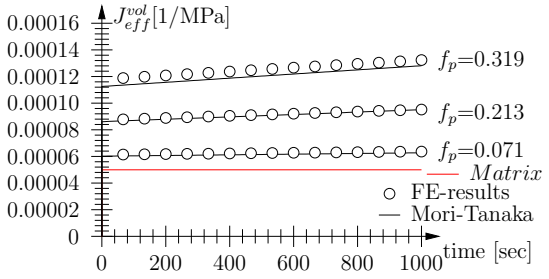

J^{vol}_{eff} for three parameter model

Figure 2.5: Comparison of the results obtained by FE and MT calculation for case ② [according to Table 2.2]

Chapter 3

Creep experiments

In this chapter, shotcrete mixtures, which have been employed in different parts of the tunnel construction project 'Lainzer Tunnel', are investigated experimentally (see Table 3.1). Hereby, the samples for the tests series II and III were taken from the construction

test series	concrete mix	additional differentiating factors
I	LT31	mixed in laboratory
II	LT31	sample taken from construction site
III	LT31	sample taken from construction site with high loading
IV	LT33	mixed in laboratory
V	LT44	mixed in laboratory

Table 3.1: Creep test series

site, whereas the samples for the remaining test series are produced in the laboratory. During testing, the cylindrical samples were loaded by a constant axial force F (see Tables 3.2 to 3.6). The change in length of each sample was recorded by four inductive

creep sample						shrinkage sample
test	t_0 [d]	L [mm]	D [mm]	axial load F [kN]	v [kN/s]	L_s [mm]
①	1.2	206	70	14.8	1.5	210
②	2.0	197	70	23.1	2.0	179
③	3.2	177	70	28.1	3.0	178

Table 3.2: Test series I: geometric properties (L: length of sample; D: diameter of sample), sample age t_0 at loading, and axial load F (L_s: length of the non-loaded shrinkage sample)

displacement transducers as depicted in Figure 3.1.

creep sample						shrinkage sample
test	t_0 [d]	L [mm]	D [mm]	axial load F [kN]	v [kN/s]	L_s [mm]
①	0.90	212	73	11.5	1.2	202
②	0.91	234	73	24.1	2.4	237
③	1.58	227	73	20.1	2.0	241
④	0.93	218	73	18.0	1.8	215
⑤	0.95	234	73	18.1	1.8	246
⑥	5.82	210	73	34.7	3.5	219

Table 3.3: Test series II: geometric properties (L: length of sample; D: diameter of sample), sample age t_0 at loading, and axial load F (L_s: length of the non-loaded shrinkage sample)

creep sample						shrinkage sample
test	t_0 [d]	L [mm]	D [mm]	axial load F [kN]	v [kN/s]	L_s [mm]
①	1.62	206	73	29.3	2.9	153
②	1.68	170	73	29.3	2.9	156
③	2.74	208	73	41.9	4.2	152
④	2.79	192	73	41.9	4.2	139

Table 3.4: Test series III: geometric properties (L: length of sample; D: diameter of sample), sample age t_0 at loading, and axial load F (L_s: length of the non-loaded shrinkage sample)

3.1 Results

The average strain $\varepsilon(t) = u(t)/L$ of each sample was obtained from the averaged values of the displacement measurements (see Figures 3.2 to 3.6). The history of the temperature T and the relative humidity h the samples were exposed during testing are documented in Figures 3.7 to 3.11.

creep sample						shrinkage sample
test	t_0 [d]	L [mm]	D [mm]	axial load F [kN]	v [kN/s]	L_s [mm]
①	1.01	169	70	19.0	1.9	182
②	1.22	197	70	20.0	2.0	191
③	1.25	176	70	15.3	1.5	203
④	2.26	179	70	22.3	2.2	193
⑤	3.15	203	70	25.8	2.6	198

Table 3.5: Test series IV: geometric properties (L: length of sample; D: diameter of sample), sample age t_0 at loading, and axial load F (L_s: length of the non-loaded shrinkage sample)

creep sample						shrinkage sample
test	t_0 [d]	L [mm]	D [mm]	axial load F [kN]	v [kN/s]	L_s [mm]
①	1.04	163	70	16.0	1.6	157
②	1.10	204	70	16.0	1.6	169
③	1.11	189	70	16.0	1.6	–
④	1.16	179	70	16.0	1.6	112

Table 3.6: Test series V: geometric properties (L: length of sample; D: diameter of sample), sample age t_0 at loading, and axial load F (L_s: length of the non-loaded shrinkage sample)

Figure 3.1: Test arrangement for uniaxial testing of shotcrete

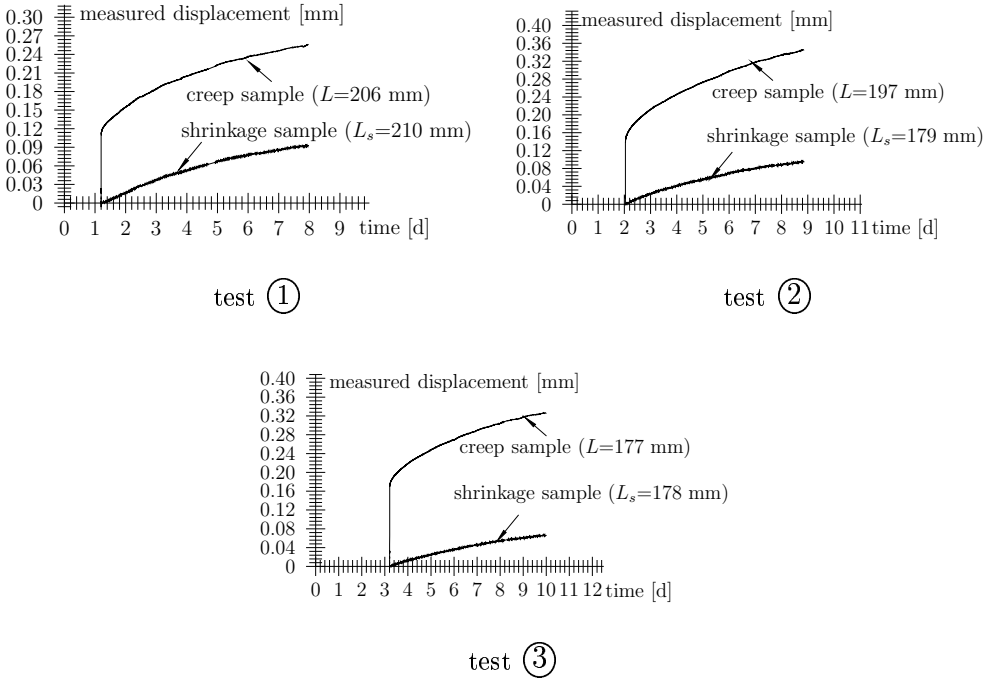

Figure 3.2: Test series I: measured displacement history for the loaded and non-loaded sample

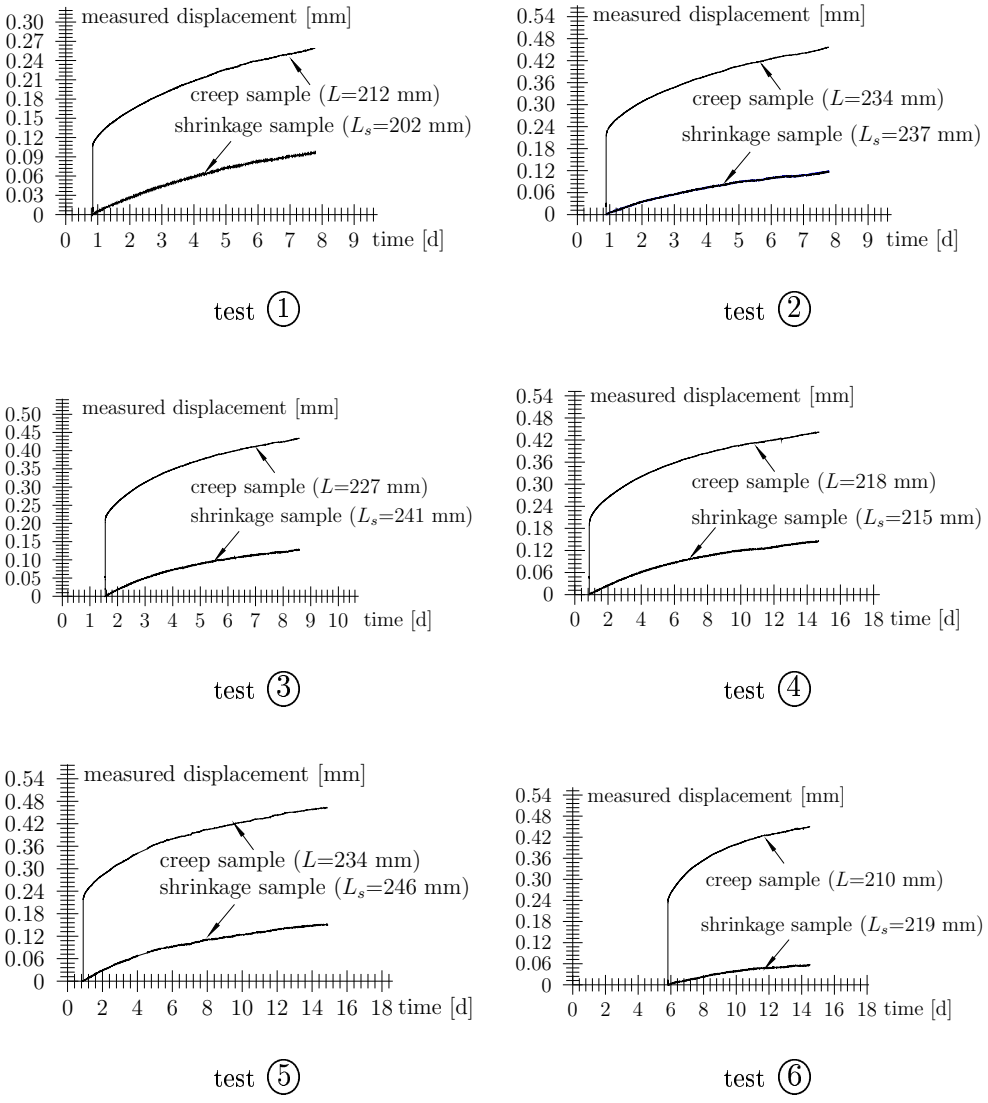

Figure 3.3: Test series II: measured displacement history for the loaded and non-loaded sample

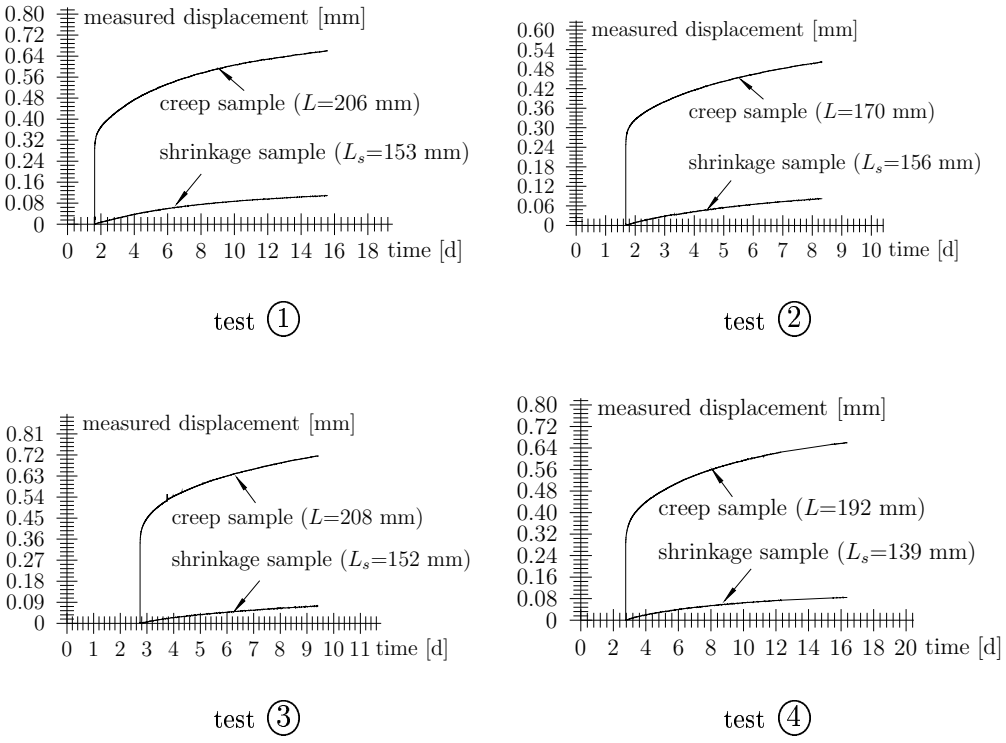

Figure 3.4: Test series III: measured displacement history for the loaded and non-loaded sample

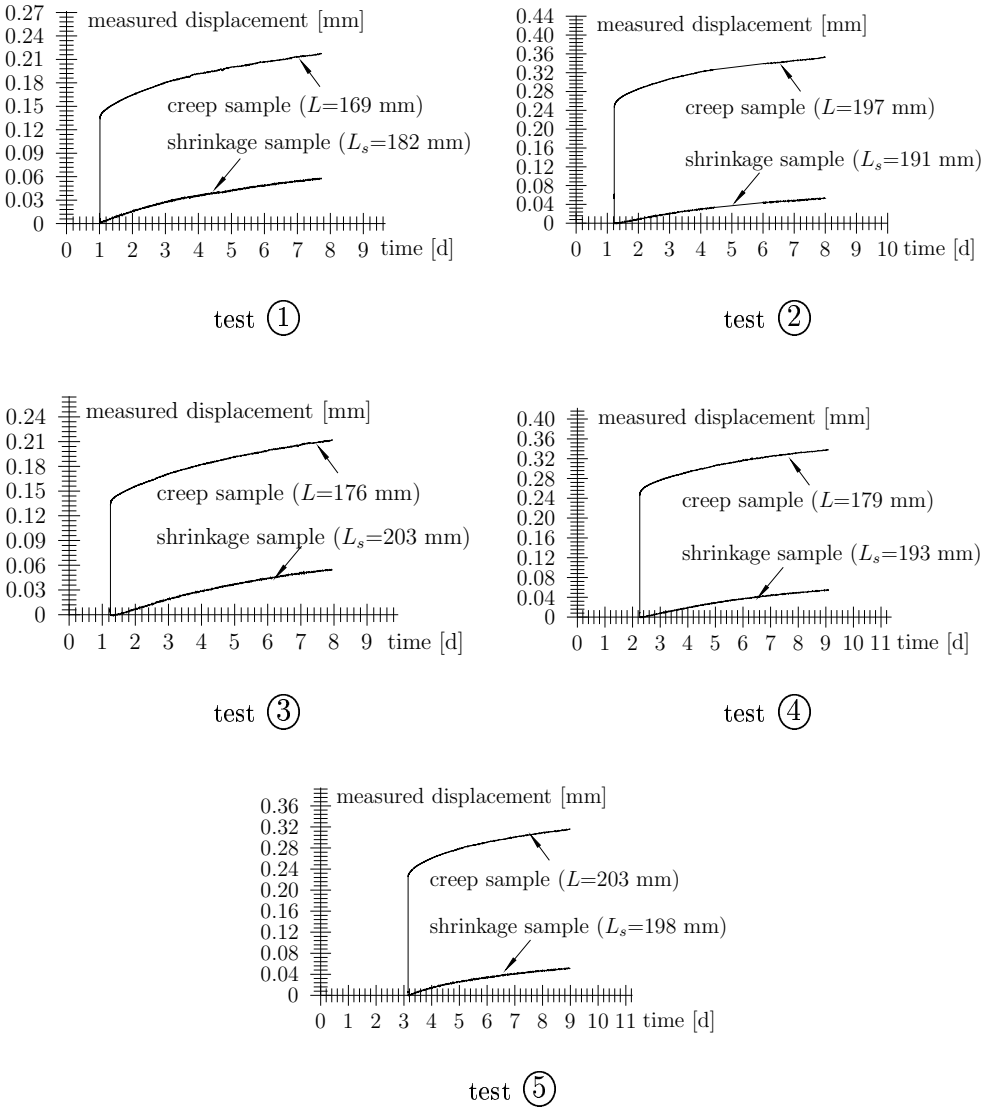

Figure 3.5: Test series IV: measured displacement history for the loaded and non-loaded sample

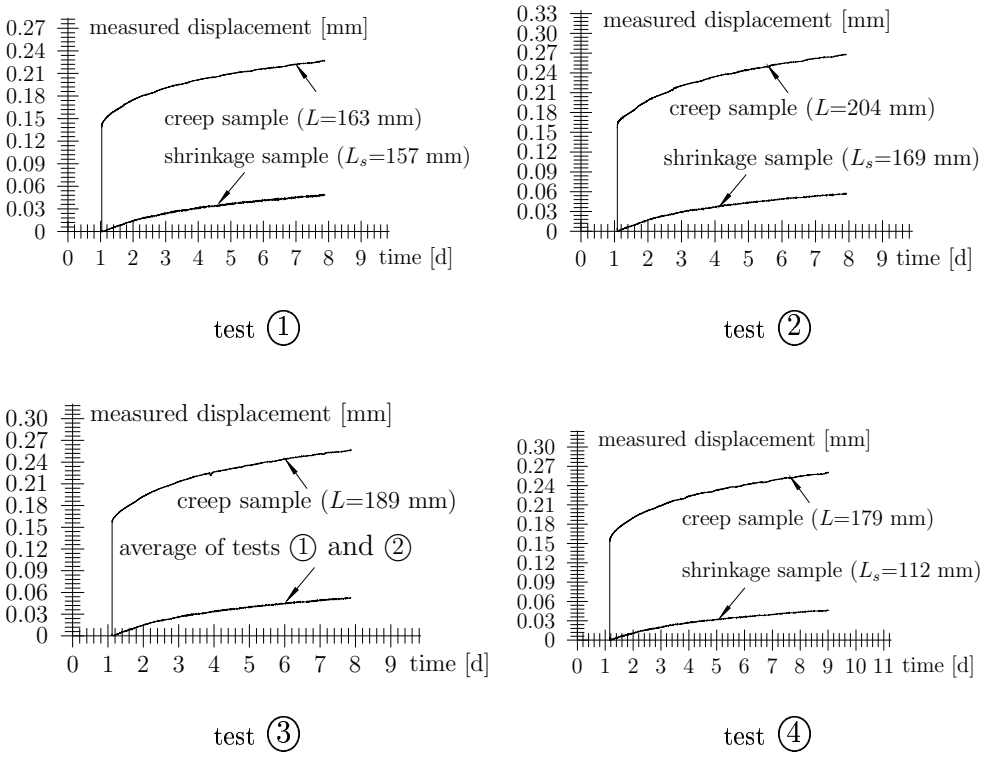

Figure 3.6: Test series V: measured displacement history for the loaded and non-loaded sample

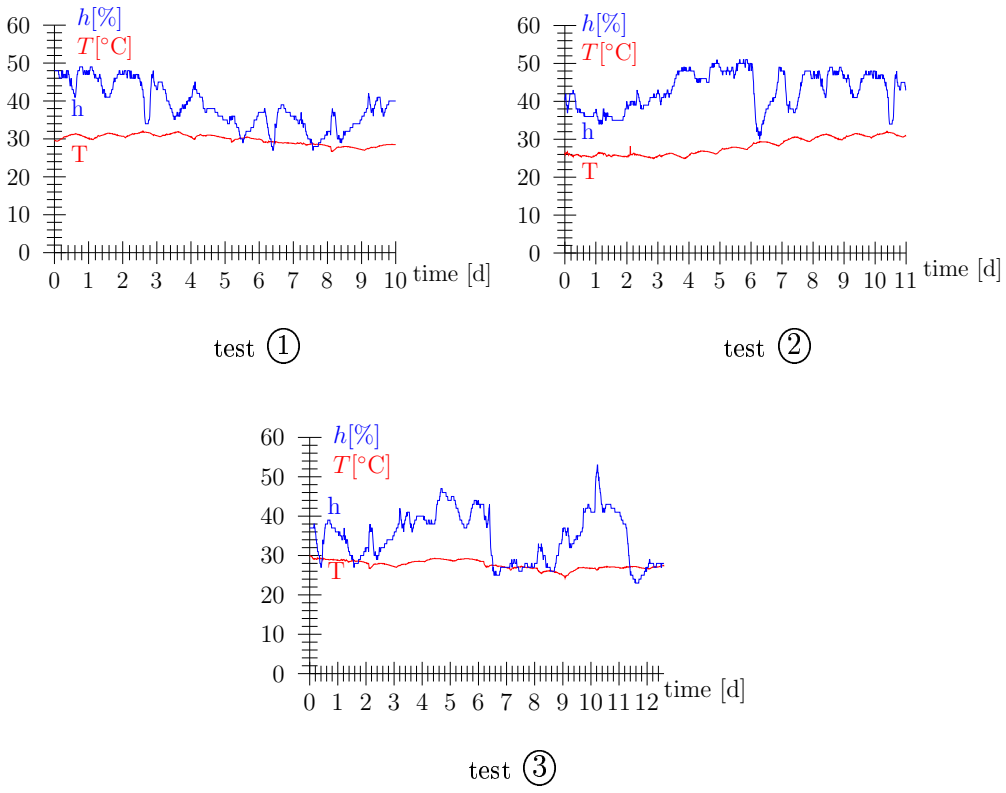

Figure 3.7: Test series I: history of temperature T and relative humidity h

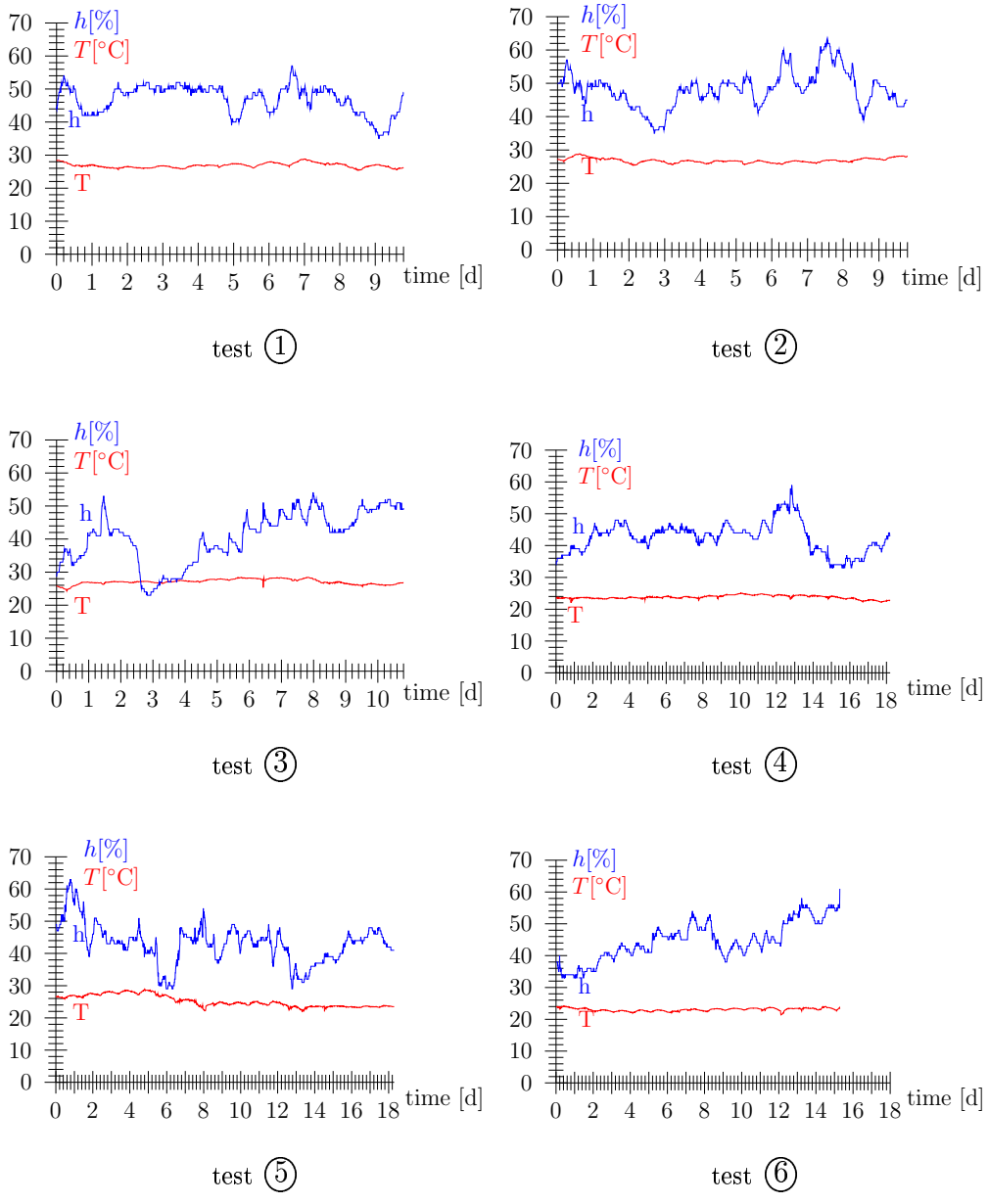

Figure 3.8: Test series II: history of temperature T and relative humidity h

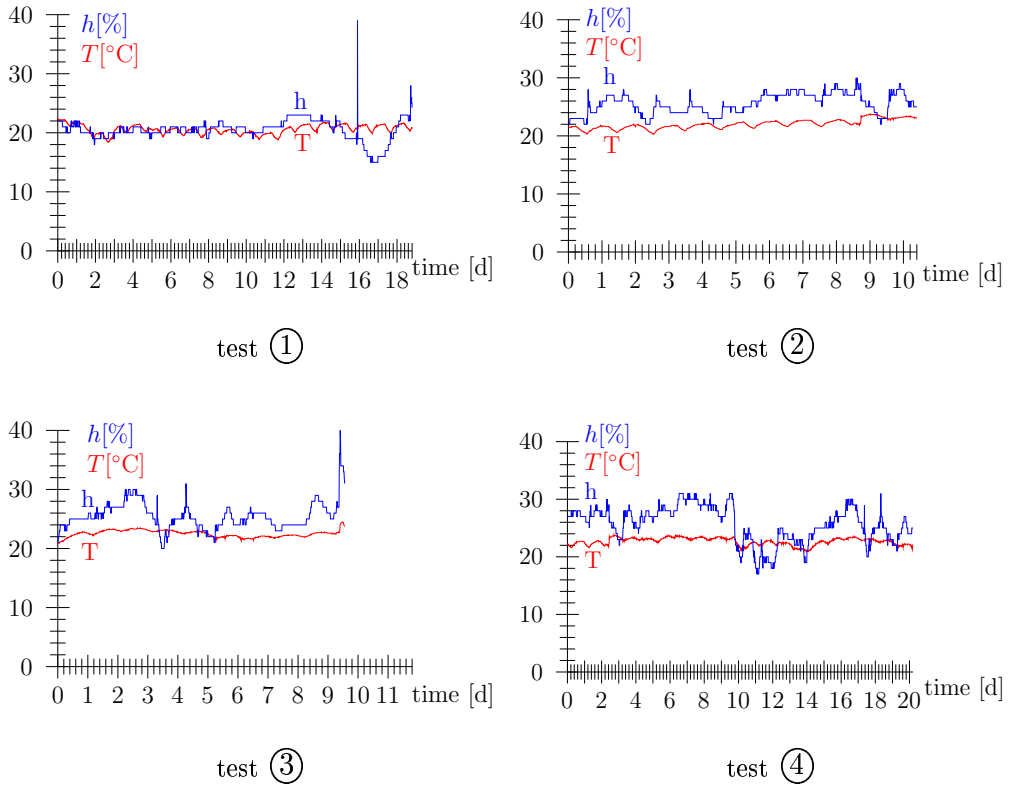

Figure 3.9: Test series III: history of temperature T and relative humidity h

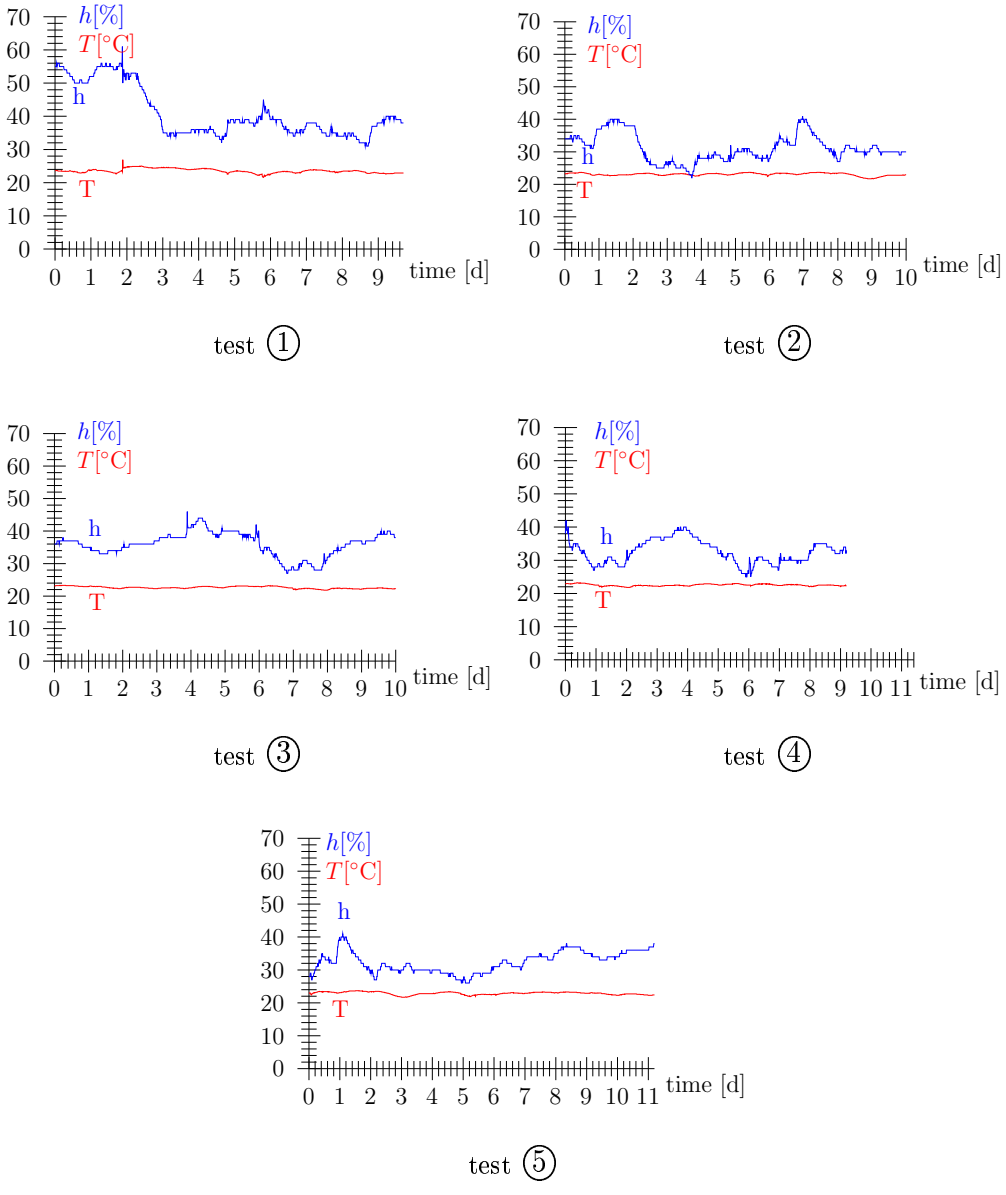

Figure 3.10: Test series IV: history of temperature T and relative humidity h

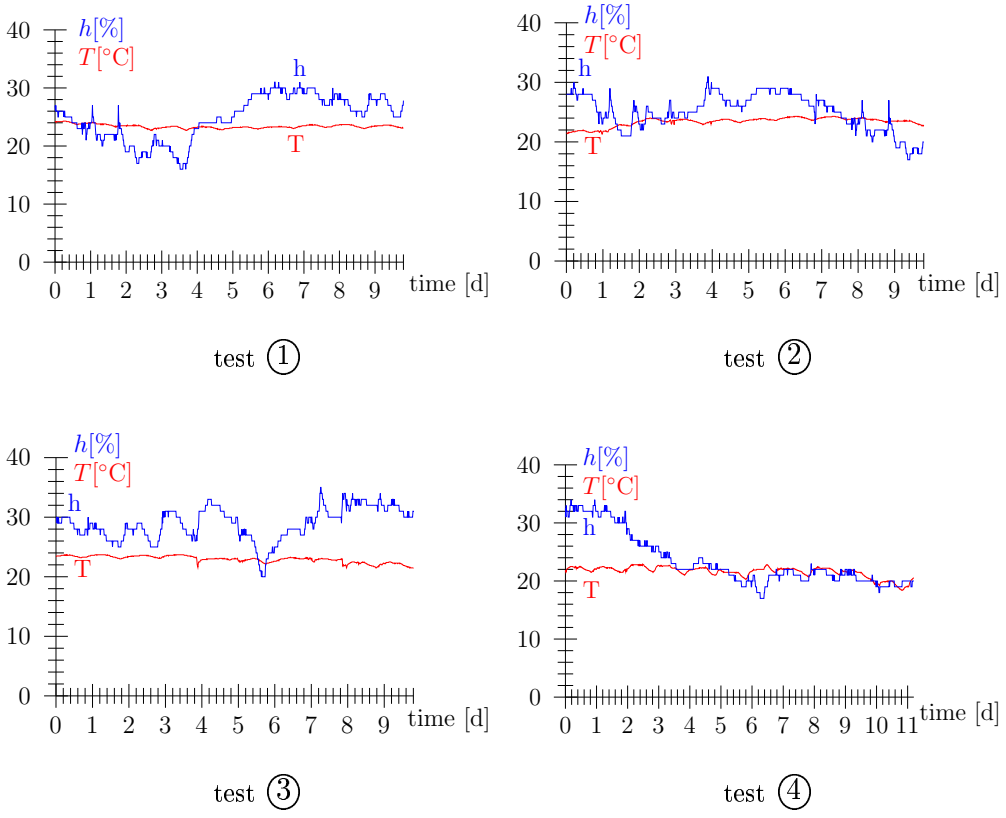

Figure 3.11: Test series V: history of temperature T and relative humidity h

3.2 Determination of creep parameters

Figure 3.12 shows the evolution of the overall degree of hydration $\xi(t,T)$ for a constant temperature $T = 30°\text{C}$ for the employed types of cement obtained from differential-calorimetry experiments. Based on the heat release $Q(t,T)$ measured during these experiments and the latent heat L_ξ, $\xi(t,T)$ is obtained as

$$\xi(t,T) = \frac{Q(t,T)}{L_\xi}, \tag{3.1}$$

where the values for L_ξ are given in Table 3.7. Using the Arrhenius law for modeling the

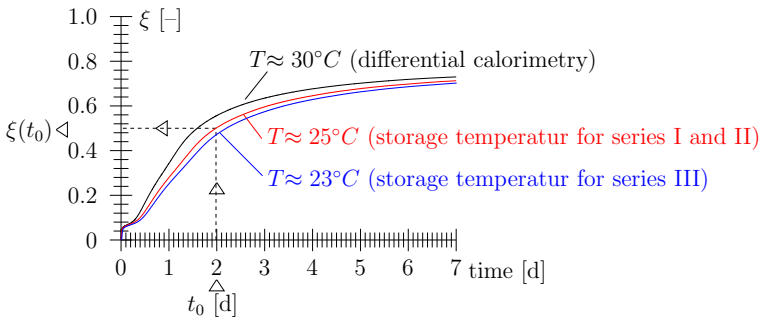

Test series I,II and III

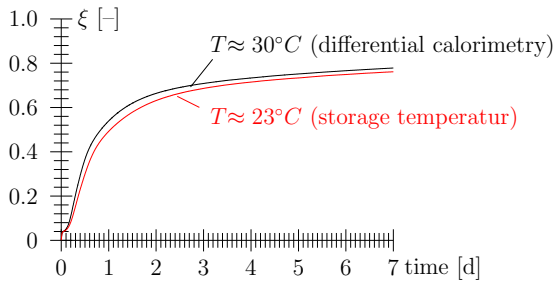

Test series IV

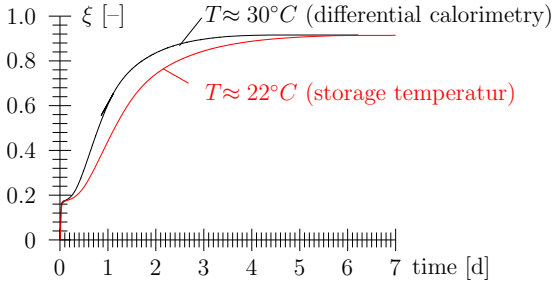

Test series V

Figure 3.12: Evolution of hydration degree $\xi(t,T)$ for $T = 30°\text{C}$ and for different storage temperatures (t_0: time instant (age) of loading)

hydration kinetics of shotcrete, with

$$\dot{\xi} = A_\xi \exp\left[-\frac{E_a}{RT}\right], \tag{3.2}$$

the chemical affinity A_ξ can be computed from the measured heat-release rate $\dot{Q}$ as

$$A_\xi = \dot{\xi}\exp\left[\frac{E_a}{RT}\right] = \frac{\dot{Q}}{L_\xi}\exp\left[\frac{E_a}{R(273+30)}\right], \tag{3.3}$$

where E_a and R denote the activation energy of the hydration process and the gas constant, respectively, with E_a/R =4000 K (see Table 3.7). In order to determine the hydration extent of the sample used in the creep experiments at the time instant of loading, $\xi(t_0)$, the evolution of the hydration extent is determined using the Arrhenius law, considering the storage temperatur T (see Figure 3.12):

$$\xi(t,T) = \frac{1}{L_\xi}\int_0^t \dot{Q} d\tau \, \exp\left[-\frac{E_a}{RT} + \frac{E_a}{R(273+30)}\right]. \tag{3.4}$$

The creep compliance $J(t,t_0)$ is determined from the measured displacement history and

	L_ξ[kJ/(kg cement)]	E_a/R[K]
LT31	475	4000
LT33	425	4000
LT44	320	4000

Table 3.7: Input parameters for determination of $\xi(t,T)$

the applied load (see Figures 3.13 to 3.17) as

$$J(t,t_0) = \frac{\varepsilon^{ve}(t)}{\sigma} = \frac{\varepsilon(t) - \varepsilon^s(t)}{F/(D^2\pi/4)} = \frac{u(t)/L - u^s(t)/L_s}{F/(D^2\pi/4)}. \tag{3.5}$$

The creep compliance $J(t,t_0)$ is composed of the elastic compliance $J_e(t_0)$, the compliance

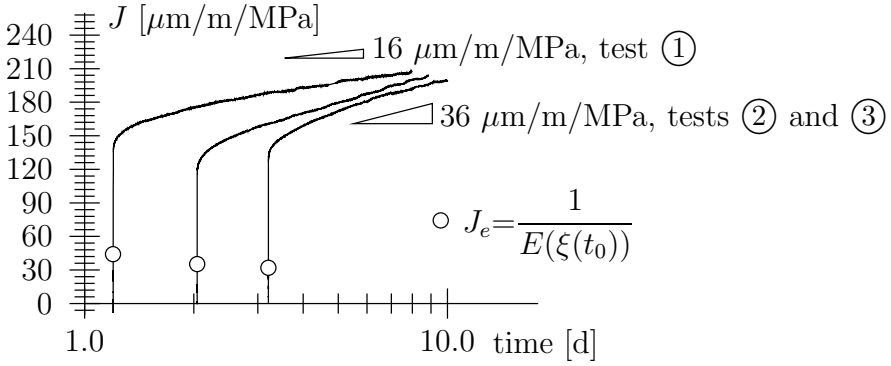

Figure 3.13: Test series I: creep compliance $J(t,t_0)$

for short-term creep $J_v(t,t_0)$, and the compliance for long-term creep $J_f(t,t_0)$:

$$J(t,t_0) = J_e(t_0) + J_v(t,t_0) + J_f(t,t_0). \tag{3.6}$$

The elastic compliance is obtained from

$$J_e(t_0) = \frac{1}{E[\xi(t_0)]}, \text{ with } E(\xi) = \sqrt{\xi}E_\infty. \tag{3.7}$$

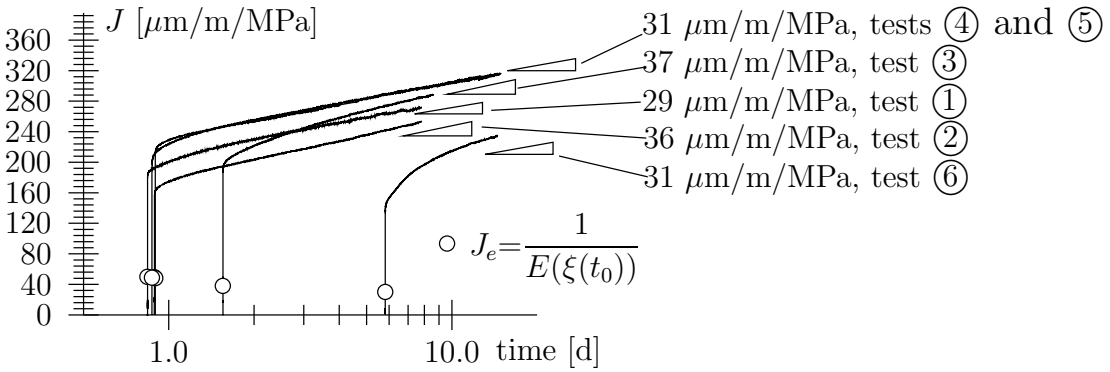

Figure 3.14: Test series II: creep compliance $J(t, t_0)$

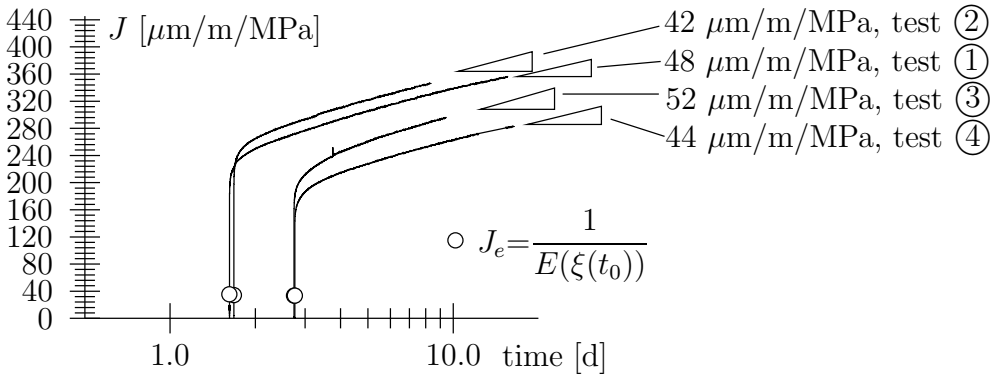

Figure 3.15: Test series III: creep compliance $J(t, t_0)$

The parameter H describing long-term creep, with

$$J_f(t, t_0) = \frac{1}{H} \ln\left(\frac{t}{t_0}\right), \tag{3.8}$$

is obtained from the creep-compliance rate $\dot{J}$ see (Figure 3.18) for $t \gg t_0$. Finally, the short-term creep compliance is obtained from $J_v = J - J_e - J_f$. For $t \gg t_0$, J_v converges to the horizontal asymptote $J_v^\infty[\xi(t_0)]$, as depicted in Figure 3.19. Figure 3.20 shows the obtained values of $J_v^\infty[\xi(t_0)]$ as a function of the hydration degree at the time instant of loading, $\xi(t_0)$. Provided that short-term creep is decaying for completed hydration, with $J_v^\infty(\xi = 1) = 0$, J_v^∞ can be approximated by

$$J_v^\infty[\xi] = J_{v,0}^\infty(1 - \xi) \quad [\mu\text{m/m/MPa}], \tag{3.9}$$

where $J_{v,0}^\infty$ is the value of J_v^∞ at $\xi = 0$. Tables 3.8 to 3.12 contain the indentified values for the creep parameters $J_{v,0}^\infty$ and $1/H$ for the tests of the conducted test series. Table 3.13 contains the average values for the creep parameters for the conducted test series.

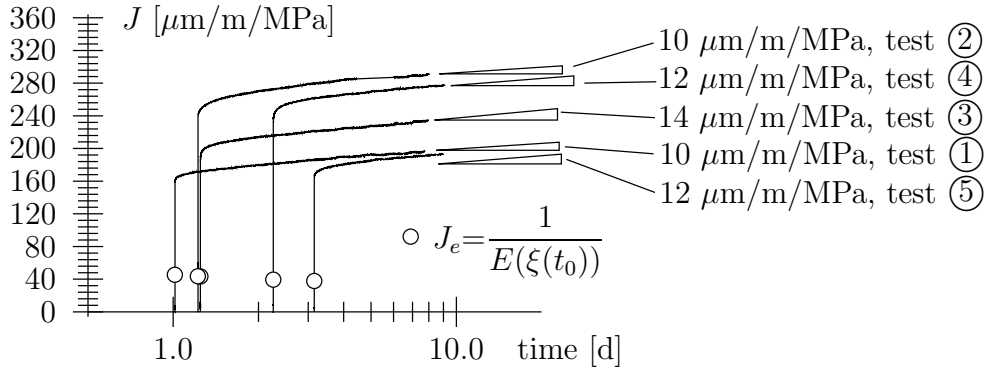

Figure 3.16: Test series IV: creep compliance $J(t, t_0)$

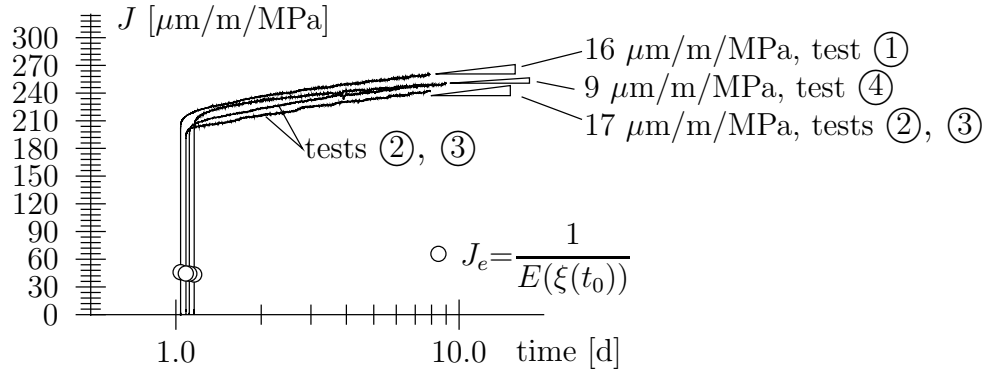

Figure 3.17: Test series V: creep compliance $J(t, t_0)$

test	$J_{v,0}^{\infty}$ [μm/m/MPa]	$1/H$ [μm/m/MPa]
①	133	16
②	116	36
③	128	36

Table 3.8: Creep parameters obtained from test series I

test	$J_{v,0}^{\infty}$ [μm/m/MPa]	$1/H$ [μm/m/MPa]
①	158	29
②	125	36
③	188	37
④	183	31
⑤	183	31
⑥	176	31

Table 3.9: Creep parameters obtained from test series II

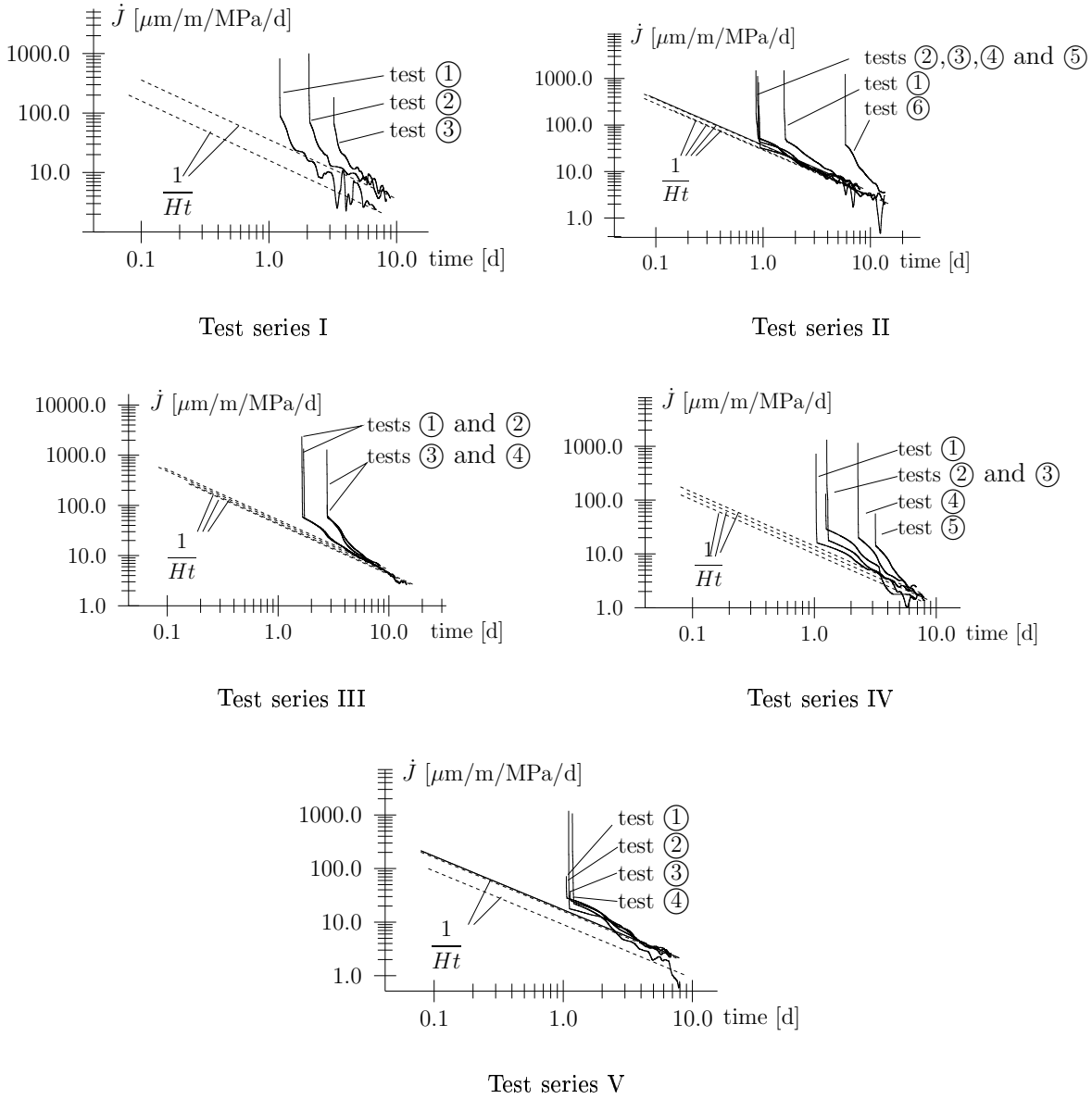

Figure 3.18: Creep compliance rate $\dot{J}$ and approximation of long-term creep by $\dot{J}_f \approx 1/(Ht)$

test	$J^{\infty}_{v,0}$ [μm/m/MPa]	$1/H$ [μm/m/MPa]
①	227	42
②	235	48
③	198	52
④	173	44

Table 3.10: Creep parameters obtained from test series III

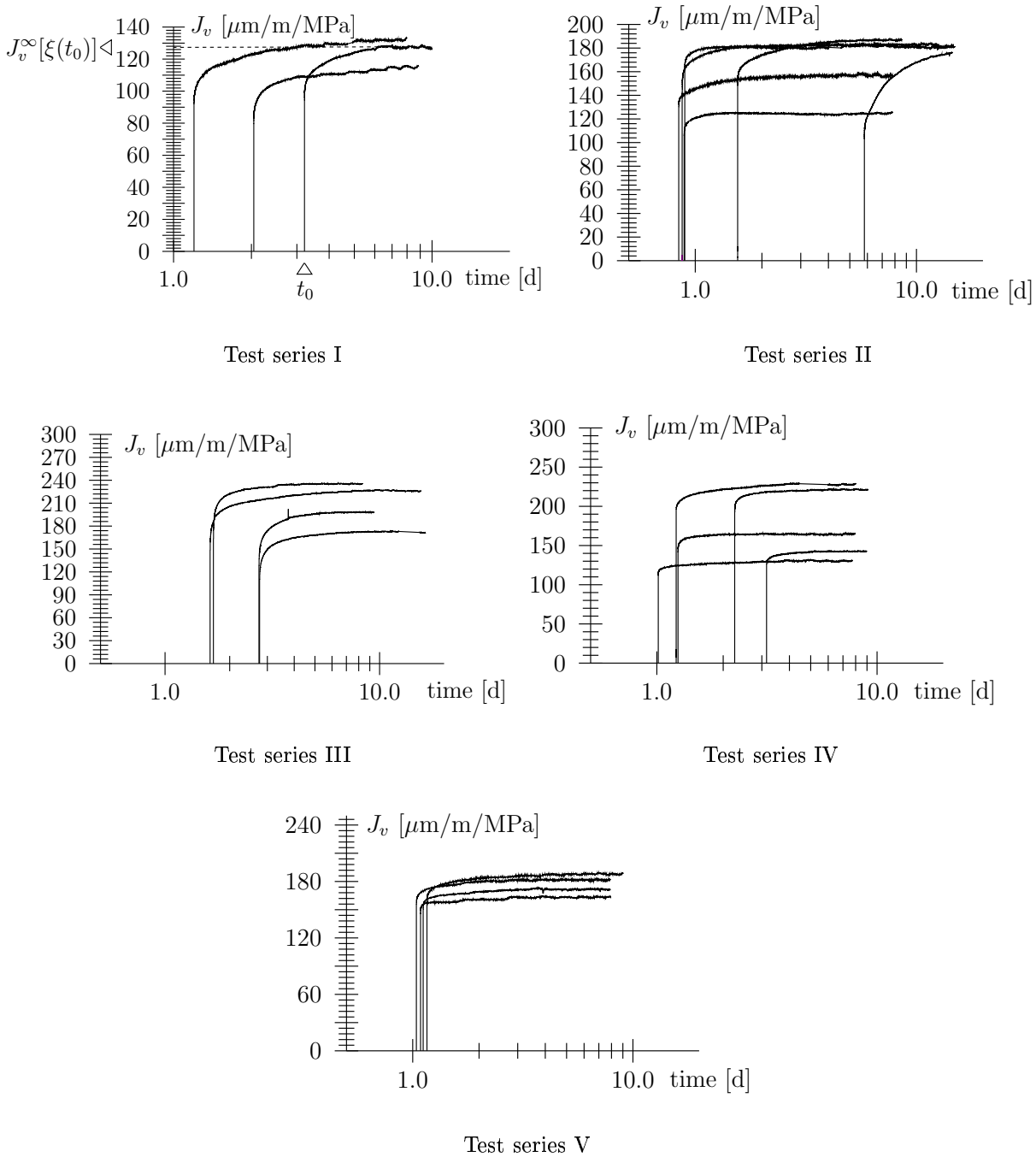

Figure 3.19: Short-term creep compliance J_v and determination of $J_v^\infty[\xi(t_0)] = J_v(t \gg t_0, t_0)$ [outlined in Figure 3.19]

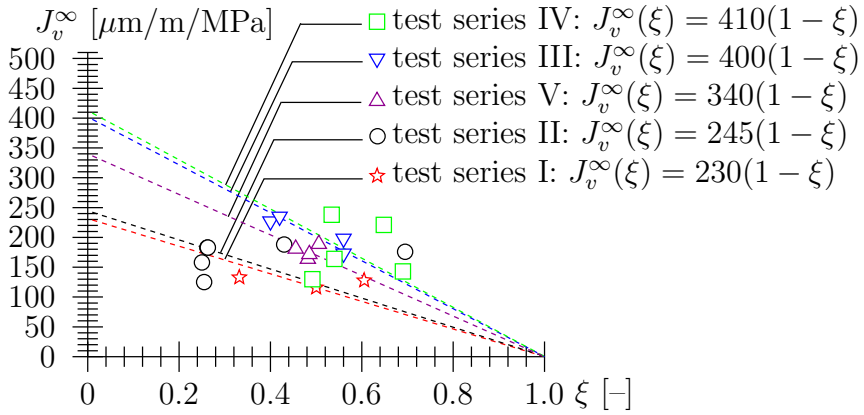

Figure 3.20: J_v^∞ as a function of the hydration degree ξ

test	$J_{v,0}^\infty$ [μm/m/MPa]	$1/H$ [μm/m/MPa]
①	130	10
②	238	10
③	164	14
④	221	12
⑤	143	12

Table 3.11: Creep parameters obtained from test series IV

test	$J_{v,0}^\infty$ [μm/m/MPa]	$1/H$ [μm/m/MPa]
①	181	16
②	164	17
③	172	17
④	189	9

Table 3.12: Creep parameters obtained from test series V

test	$J_{v,0}^\infty(\xi = 0)$ [μm/m/MPa]	$1/H$ [μm/m/MPa]
I	230	30
II	245	32
III	400	47
IV	410	12
V	340	15

Table 3.13: Average values for creep parameters for conducted test series

3.3 Comparison with micromechanical model

The multiscale model outlined in Appendix A was applied to the tested types of shotcrete with the input parameters listed in Table 3.14. The results of these calculations are com-

	unit	LT31	LT33	LT44
water/cement-value	[-]	0.529	0.442	0.551
aggregate/cement-value	[-]	4.5	3.9	5.4
cement	[kg/m^3]	378	430	350
ambient temperate	[°C]	25	22	23
Young's modulus of the aggregate	[GPa]	50	50	50
Poisson ratio of the aggregate	[-]	0.3	0.3	0.3
Blaine	[cm^2/g]	4850	4500	4300
radius of the cement grain	[μm]	5	7	12
C3S-ratio	[mass-%]	65.7	62.3	46.3
C2S-ratio	[mass-%]	11.8	9.5	25.9
C3A-ratio	[mass-%]	7.1	5.1	9.6
C4AF-ratio	[mass-%]	6.2	5.1	7.0
gypsum-ratio	[mass-%]	5.0	5.6	3.0
other	[mass-%]	4.2	12.4	10.9

Table 3.14: Input-parameter set for multiscale model

pared with the experimentally-obtained results as depicted in Figures 3.21 to 3.24. For the LT31 shotcrete, the multiscale model underestimates both the short-term and the long-term creep behavior (see Figure 3.21). This could be explained (i) by some additives as accelerators or the FLUAMIX C mixture added to the LT31 shotcrete, (ii) by the more-than-average rebound of larger aggregates during application of shotcrete onto the tunnel wall, increasing the cement/aggregate-ratio of the shotcrete, and (iii) by the larger amount of air voids introduced during shotcrete application. As regards the rebound of larger aggregates, the creeping cement-paste phase would have more impact on the behavior of the shotcrete, resulting in a more pronounced creep behavior. Therefore the calculations were repeated considering a cement content of 750 kg/m^3 instead of 378 kg/m^3, as depicted in Figure 3.22.

The results for the LT33 shotcrete are agreeing much better with the experimentally-obtained results, especially as regards long-term creep. As already mentioned, the samples for LT33 and LT44 were mixed in the laboratory. So any effects caused by the application of the shotcrete were excluded. For the LT33 shotcrete, an accelerator was used which is not considered in the underlying hydration model outlined in Appendix A. Accordingly, the agreement between the experimental results and the multiscale-model prediction is the best for the LT44 shotcrete, not containing any accelerators.

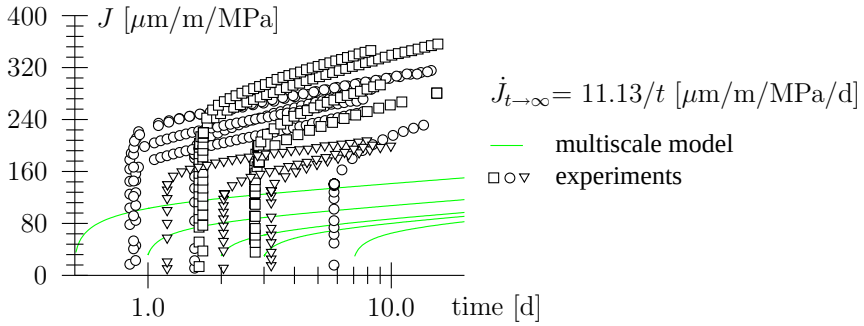

Figure 3.21: LT31: Comparison of the experimental results with the multiscale-model prediction (378 kg cement/m^3 shotcrete)

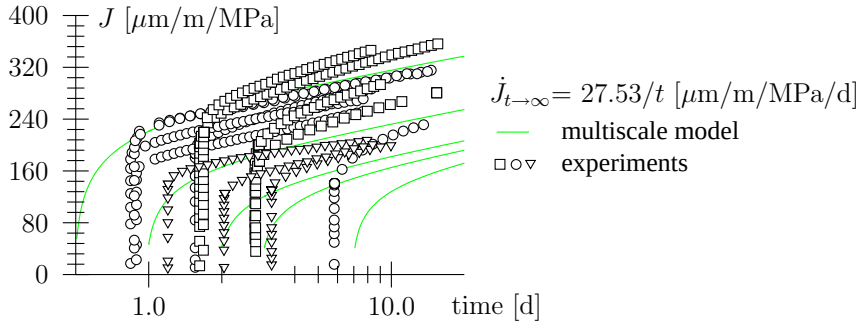

Figure 3.22: LT31: Comparison of the experimental results with the multiscale-model prediction (750 kg cement/m^3 shotcrete)

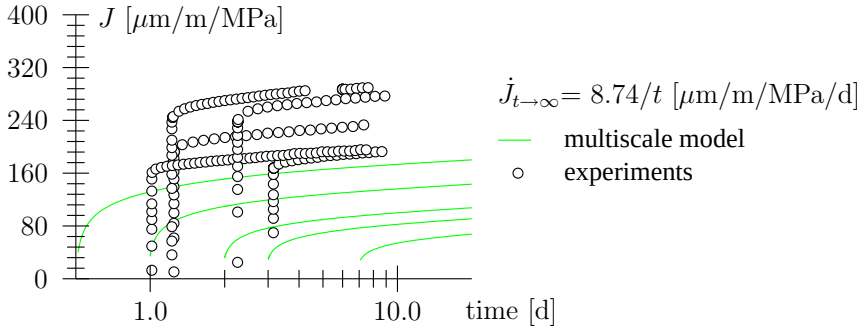

Figure 3.23: LT33: Comparison of the experimental results with the multiscale-model prediction

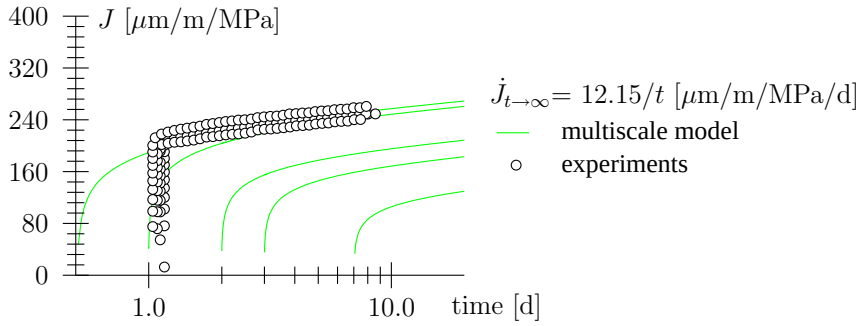

Figure 3.24: LT44: Comparison of the experimental results with the multiscale-model prediction

Bibliography

[1] J. L. Auriault and E. Sanchez-Palencia. Etude du comportement macroscopique d'un milieu poreux saturé déformable [Study on the macroscopic behavior of a saturated deformable porous medium]. *Journal de Mécanique*, 16(4):575–603, 1977. In French.

[2] O. Bernard, F.-J. Ulm, and E. Lemarchand. A multiscale micromechanics-hydration model for the early-age elastic properties of cement-based materials. *Cement and Concrete Research*, 33:1293–1309, 2003.

[3] S. Beurthey and A. Zaoui. Structural morphology and relaxation spectra of viscoelastic heterogenous materials. *European Journal of Mechanics A/Solids*, 19:1–16, 2000.

[4] H.R. Chen, Yang Q.S., and Williams F.W. A self-consistent finite element approach to the inclusion problem. *Computational Material Science*, 2:301–307, 1994.

[5] J. D. Eshelby. The determination of the elastic field of an ellipsoidal inclusion, and related problems. *Proceedings of the Royal Society of London A*, 241:376–396, 1957.

[6] K. Fuji and W. Kondo. Kinetics of the hydration of tricalcium silicate. *Journal of the American Ceramic Society*, 57:492–502, 1974.

[7] D. Gross and Th. Seelig. *Bruchmechanik [Fracture mechanics]*. Springer, Berlin, 3rd edition, 2001. In German.

[8] A. V. Hershey. The elasticity of an isotropic aggregate of anisotropic cubic crystals. *Journal of Applied Mechanics (ASME)*, 21:236–240, 1954.

[9] C. Huet. Application of variational concepts to sizes effects in elastic heterogeneous bodies. *Journal of the Mechanics and Physics of Solids*, 38:813–841, 1990.

[10] E. Kroener. Berechnung der elastischen Konstanten des Vielkristalls aus den Konstanten des Einkristalls [Computation of the elastic constants of a polycrystal based on the constants of the single crystal]. *Zeitschrift für Physik*, 151:504–518, 1958. In German.

[11] N. Laws and R. E. McLaughlin. Self-consistent estimates for the viscoelastic creep compliance of composite materials. *Proceedings of the Royal Society of London A*, 359:251–273, 1978.

[12] C. K. Lee, C. C. Sun, and C. C. Mei. Computation of permeability and dispersivities of solute or heat in periodic porous media. *International Journal of Heat and Mass Transfer*, 39(4):661–676, 1996.

[13] J. Mandel. *Mécanique des milieux continus [Continuum mechanics]*. Gauthier, Paris, 1966. In French.

[14] T. Mori and K. Tanaka. Average stress in matrix and average elastic energy of materials with misfitting inclusions. *Acta Metallurgica*, 21:571–574, 1973.

[15] S. B. Moser. *Vollautomatisierung der Spritzbetonapplikation – Entwicklung der Applikations-Prozesssteuerung*. Girmscheid, Zürich, 1st edition, 2004.

[16] Ch. Pichler. *Multiscale characterization and modeling of creep and autogenous shrinkage of early-age cement-based materials*. PhD thesis, Vienna University of Technology, 2007.

[17] J. Pommersheim and J. Chang. Kinetics of hydration of tricalcium aluminate in the presence of gypsum. *Cement and Concrete Research*, 18:911–922, 1988.

[18] F.G. Rammerstorfer and H.J. Böhm. Composites engineering – part 2: Continuum micromechanics of materials,. Technical report.

[19] E. Sanchez-Palencia. Comportements local et macroscopique d'un type de milieux physiques heterogenes [Local and macroscopic behavior of a heterogenous media]. *International Journal of Engineering Science*, 12(4):331–351, 1974.

[20] M. Sautter, C. Dietrich, M.H. Poech, S Schmauder, and H.F. Fischmeister. Finite element modelling of a transverse-loaded fibre composite: Effects of section size and net density. *Computational Material Science*, 1:225–233, 1993.

[21] P. Suquet, editor. *Continuum micromechanics*. Springer, Vienna, 1997.

[22] P. Suquet. Effective properties of nonlinear composites. In P. Suquet, editor, *Continuum micromechanics*. Springer, Vienna, 1997.

[23] P. D. Tennis and H. M. Jennings. A model for two types of calcium silicate hydrate in the microstructure of Portland cement pastes. *Cement and Concrete Research*, 30:855–863, 2000.

[24] K. Váradi, Z. Néder, K. Friedrich, and J. Flöck. Finite-element analysis of a polymer composite subjected to ball indentation. *Composites Science and Technology*, 59:271–281, 1999.

[25] A. Zaoui. Structural morphology and constitutive behaviour of microheterogenous materials. In P. Suquet, editor, *Continuum micromechanics*. Springer, Vienna, 1997.

Appendix A

Multiscale model according to [16]

A.1 Observation scales

The multiscale model for upscaling of viscoelastic properties consists of four length scales:

- Scale I comprises the four clinker phases, high-density CSH (CSH-HD) and low-density CSH (CSH-LD), and the water and air phase. The four clinker phases, which do not exhibit time-dependent behavior, are condensed into one material phase (Scale Ia). The constituents showing time-dependent behavior, on the other hand, are combined at Scale Ib-1, where CSH-HD is located in the space confined by the previously formed CSH-LD. At the porous CSH scale (Scale Ib-2), water and air are considered as inclusions in a matrix constituted by the homogenized material of Scale Ib-1.

- At Scale II (*cement-paste scale*), anhydrous cement (homogenized material of Scale Ia), gypsum $C\bar{S}H_2$, portlandite CH, and reaction products from C_3A and C_4AF hydration form inclusions in a matrix constituted by the homogenized material of Scale Ib-2.

- At Scale III (*mortar* or *concrete scale*), aggregates are represented as inclusions in the cement paste (homogenized material of Scale II).

- Finally, at Scale IV (*macroscale*), concrete is treated as a continuum, characterized by customary material properties, such as Young's modulus, Poisson's ratio, and compressive strength.

The four length scales obey the separability of scale condition, i.e., they are separated one from each other by at least one order of magnitude. For upscaling of information from the finer scales towards the macroscale, continuum micromechanics is employed. Hereby, the self-consistent scheme [10, 8] is used for homogenization at Scale Ia. For homogenization at Scales Ib to III the matrix-inclusion type morphology is taken into account by using the Mori-Tanaka homogenization scheme [14]. The volume fractions at the different length

scales entering the homogenization schemes are obtained from the hydration model outlined in the following subsection.

A.2 Hydration model

For determination of the volume fractions of the phases of early-age cement paste, the following set of stoichiometric reactions are employed for the four main clinker phases of Portland cement, i.e., tricalcium silicate (C_3S), dicalcium silicate (C_2S), tricalcium aluminate (C_3A), and tetracalcium aluminate ferrite (C_4AF) [23]:

$$C_3S + 5.3\,H \rightarrow 0.5\,C_{3.4}S_2H_8 + 1.3\,CH \quad (A.1)$$

$$C_2S + 4.3\,H \rightarrow 0.5\,C_{3.4}S_2H_8 + 0.3\,CH \quad (A.2)$$

$$C_4AF + 2\,CH + 10\,H \rightarrow 2\,C_3(A,F)H_6 \quad (A.3)$$

$$C_3A + 3\,C\bar{S}H_2 + 26\,H \rightarrow C_6A\bar{S}_3H_{32} \quad (A.4)$$

$$C_3A + 0.5\,C_6A\bar{S}_3H_{32} + 2\,H \rightarrow 1.5\,C_4A\bar{S}H_{12} \quad (A.5)$$

$$C_3A + CH + 12\,H \rightarrow C_4AH_{13} \quad (A.6)$$

Equations (A.4) to (A.6) describe the formation of calcium aluminate hydrates from C_3A in the presence of gypsum, which is added to prevent rapid setting of C_3A. Initially, C_3A reacts with gypsum to form ettringite [Equation (A.4)]. After all gypsum is consumed, C_3A reacts with the previously formed ettringite to form monosulfoaluminates [Equation (A.5)]. Following depletion of the ettringite supply, C_3A reacts with portlandite CH (one of the products of C_3S and C_2S hydration). The hydration extent is described by the degree of hydration of the clinker phases, ξ_{C_3S}, ξ_{C_2S}, ξ_{C_3A}, and ξ_{C_4AF}. The evolution of ξ_x ($x \in \{C_3S, C_2S, C_4AF\}$) is controlled by induction, nucleation, and growth until $\xi_x = \bar{\xi}_x$, and diffusion-limited kinetics thereafter [2]. The aforementioned three stages of C_3A hydration are diffusion limited [17].

For the description of the hydration kinetics of C_3S, C_2S, and C_4AF, kinetic laws given in [16] [2], including the Avrami law for nucleation and growth kinetics, and the Fuji & Kondo model [6] for diffusion limited kinetics, are employed. Whereas the first and the third stage of C_3A hydration are characterized by a thickening barrier layer (ettringite and C_4AH_{13}, respectively, around the anhydrous C_3A grain) and, hence, by a decreasing reaction rate, the second stage is dominated by a thinning barrier layer (ettringite) with an increasing reaction rate.

Based on the stoichiometric reactions given in Equations (A.1) to (A.6), and the molar masses $\mathcal{M}$ and densities ρ of the different phases given in [23] (see Table A.1), the volume fractions of the different phases (at the cement-paste scale) can be determined as a function of the hydration degrees ξ_x and the mass fractions of the clinker phases m_x. This is shown exemplarily for the volume fraction of $C_{3.4}S_2H_8$ appearing in Equations (A.1) and (A.2):

$$f_{C_{3.4}S_2H_8}(t) = \left[\xi_{C_3S}(t)\frac{m_{C_3S}}{\mathcal{M}_{C_3S}}\frac{0.5\mathcal{M}_{C_{3.4}S_2H_8}}{\rho_{C_{3.4}S_2H_8}} + \xi_{C_2S}(t)\frac{m_{C_2S}}{\mathcal{M}_{C_2S}}\frac{0.5\mathcal{M}_{C_{3.4}S_2H_8}}{\rho_{C_{3.4}S_2H_8}}\right]\bar{\rho}\ , \quad (A.7)$$

		density ρ [kg/m^3]	molar mass $\mathcal{M}$ [kg/mol]
tricalcium silicate	C_3S	3150	0.228
dicalcium silicate	C_2S	3280	0.172
tricalcium aluminate	C_3A	3030	0.270
tetracalcium aluminate ferrite	C_4AF	3730	0.486
water	H	998	0.018
gypsum	$C\bar{S}H_2$	2320	0.172
calcium hydroxide	CH	2240	0.074
hydrogarnet	$C_3(A,F)H_6$	2670	0.407
trisulfate ettringite	$C_6A\bar{S}_3H_{32}$	1750	1.255
monosulfate	$C_4A\bar{S}H_{12}$	1990	0.623
calcium aluminate hydrate	C_4AH_{13}	2050	0.560
calcium silicate hydrate	$C_{3.4}S_2H_8$	1990	0.454

Table A.1: Molar masses $\mathcal{M}$ and densities ρ of different phases given in cement paste (taken from [23])

with

$$\bar{\rho} = \frac{1}{\sum_x \frac{m_x}{\rho_x} + \frac{w/c}{\rho_H} \sum_x m_x} \,, \tag{A.8}$$

where w/c denotes the water/cement-(mass)ratio. The volume fractions at the mortar scale are obtained from commonly know mix characteristics, i.e., w/c, the aggregate/cement-(mass)ratio a/c, and the cement content c [kg/m^3]. The volume fraction of cement paste at Scale III is determined as

$$f_{cp} = \frac{c}{\rho_{cem}} + w/c \frac{c}{\rho_H} \,, \tag{A.9}$$

with ρ_{cem} and ρ_H denoting the density of anhydrous cement and water, respectively. On the other hand, the volume fraction of aggregates is obtained as

$$f_a = 1 - f_{cp} \,. \tag{A.10}$$

Based on the values of ξ_x determined from the kinetic laws outlined in [16], an overall degree of hydration, ξ, is computed as

$$\xi = \frac{\sum_x m_x \, \xi_x}{\sum_x m_x} \,, \tag{A.11}$$

where $x \in \{C_3S, C_2S, C_3A, C_4AF, C\bar{S}H_2\}$ and m_x representing the mass fractions of the x-th material phase. Hereby, $\xi_{C\bar{S}H_2}$ is linearly coupled to ξ_{C_3A} [see Equation (A.4)].

The input parameters for the hydration kinetic law for ordinary Portland cement [2] listed in [16] for various types of concrete taken from the open literature are the *Blaine*, i.e., the grinding fineness, the medium initial radius of the clinker grains, the mass fractions of the clinker phases m_x, and the w/c-ratio [2].

Appendix B

Upscaling of early-age basic creep according to [16]

B.1 Upscaling of elastic properties

Homogenization schemes based on continuum micromechanics consider a representative volume element (RVE) subjected to a homogeneous strain $\mathbf{E}$ at its boundary. These schemes depart from the definition of the so-called strain-localization tensor $\mathbb{A}$, linking the effective strain tensor $\mathbf{E}$ with the local strain tensor $\boldsymbol{\varepsilon}$ at the location $\mathbf{x}$:

$$\boldsymbol{\varepsilon}(\mathbf{x}) = \mathbb{A}(\mathbf{x}) : \mathbf{E} \ . \tag{B.1}$$

The effective strain tensor $\mathbf{E}$ represents the volume average of the local strain tensor $\boldsymbol{\varepsilon}$:

$$\mathbf{E} = \langle \boldsymbol{\varepsilon}(\mathbf{x}) \rangle_V = \frac{1}{V} \int_V \boldsymbol{\varepsilon}(\mathbf{x}) dV \ . \tag{B.2}$$

Inserting Equation (B.1) into Equation (B.2), one gets $\mathbf{E} = \langle \mathbb{A}(\mathbf{x}) \rangle_V : \mathbf{E}$ and, thus, $\langle \mathbb{A}(\mathbf{x}) \rangle_V = \mathbb{I}$. Considering an ellipsoidal inclusion i embedded in a reference medium characterized by the material tensor $\mathbb{c}_0$, the strain-localization tensor $\mathbb{A}$ within the domain i is constant and given by [5]

$$\mathbb{A}_i = [\mathbb{I} + \mathbb{S}_i : (\mathbb{c}_0^{-1} : \mathbb{c}_i - \mathbb{I})]^{-1} : \left\{ \sum_{r=0,i} f_r [\mathbb{I} + \mathbb{S}_r : (\mathbb{c}_0^{-1} : \mathbb{c}_r - \mathbb{I})]^{-1} \right\}^{-1} = \text{const.} \ , \tag{B.3}$$

with $\mathbb{c}_i$ as the material tensor of the inclusion i and $\mathbb{c}_0$ as the material tensor of the reference medium. $\mathbb{S}_i$ denotes the Eshelby tensor, conditioned by the geometric properties of the inclusion and the elastic properties of the reference medium.

The volume average of the local stress tensor $\boldsymbol{\sigma}(\mathbf{x})$ determines the effective stress tensor Σ:

$$\Sigma = \langle \boldsymbol{\sigma}(\mathbf{x}) \rangle_V = \frac{1}{V} \int_V \boldsymbol{\sigma}(\mathbf{x}) dV \ . \tag{B.4}$$

Considering a linear-elastic constitutive law for the r-th material phase, linking the local strain tensor with the local stress tensor,

$$\boldsymbol{\sigma}_r(\mathbf{x}) = \mathbb{c}_r : \boldsymbol{\varepsilon}_r(\mathbf{x}), \tag{B.5}$$

and Equation (B.1) in Equation (B.4) one gets

$$\Sigma = \langle \mathbb{c}(\mathbf{x}) : \mathbb{A}(\mathbf{x}) \rangle_V : \mathbf{E} \ . \tag{B.6}$$

Comparison with $\Sigma = \mathbb{C}_{eff} : \mathbf{E}$[1] gives access to the effective material tensor $\mathbb{C}_{eff}$:

$$\mathbb{C}_{eff} = \langle \mathbb{c}(\mathbf{x}) : \mathbb{A}(\mathbf{x}) \rangle_V \ . \tag{B.7}$$

Considering the morphology of the composite material, the unknown strain localization tensor $\mathbb{A}$, which so far is available for a single inclusion [Equation (B.3)], can be estimated based on the choice of $\mathbb{c}_0$. In case of a microstructure being characterized by a distinct matrix/inclusion-type morphology, which is the case e.g. at the *mortar scale* , $\mathbb{c}_0$ is set equal to the material tensor of the matrix material $\mathbb{c}_m$. This estimation leads to the Mori-Tanaka (MT) scheme [14]. Using

$$\langle \mathbb{A}(\mathbf{x}) \rangle_V = \frac{V_0}{V} \langle \mathbb{A}(\mathbf{x}) \rangle_{V_0} + \frac{V_i}{V} \langle \mathbb{A}(\mathbf{x}) \rangle_{V_i} = \mathbb{I} \quad \rightarrow \quad f_0 \langle \mathbb{A}(\mathbf{x}) \rangle_{V_0} = \mathbb{I} - f_i \mathbb{A}_i \ , \tag{B.8}$$

where $\langle \mathbb{A}(\mathbf{x}) \rangle_{V_i} = \mathbb{A}_i = \text{const.}$ was used and f_i and f_0 denote the volume fractions of the inclusion and reference medium, respectively, and Equation (B.3), one gets the volume average of the localization tensor over the reference medium as[2]

$$\langle \mathbb{A}(\mathbf{x}) \rangle_{V_0} = \left\{ \sum_{r \in 0,i} f_r \left[\mathbb{I} + \mathbb{S}_r : \left(\mathbb{c}_0^{-1} : \mathbb{c}_r - \mathbb{I} \right) \right]^{-1} \right\}^{-1} \ . \tag{B.10}$$

Considering Equations (B.10) and (B.3) in Equation (B.7) gives access to the effective

[1] *Levin's* theorem states that the effective state equation is of the same form as the local state equation [25].

[2]
$$\begin{aligned} f_0 \langle \mathbb{A}(\mathbf{x}) \rangle_{V_0} &= \mathbb{I} - f_i [\square]^{-1} : \{\bullet\}^{-1} \\ &= \{\bullet\} : \{\bullet\}^{-1} - f_i [\square]^{-1} : \{\bullet\}^{-1} \\ &= \left(\{\bullet\} - f_i [\square]^{-1} \right) : \{\bullet\}^{-1} \\ &= \left(f_0 [\mathbb{I} + \mathbb{S}_0 : (\mathbb{c}_0^{-1} : \mathbb{c}_0 - \mathbb{I})]^{-1} + f_i [\square]^{-1} - f_i [\square]^{-1} \right) : \{\bullet\}^{-1} \\ &= f_0 \{\bullet\}^{-1} \end{aligned} \tag{B.9}$$

with the abbreviations $\{\bullet\} = \left\{ \sum_{r=0,i} f_r [\mathbb{I} + \mathbb{S}_r : (\mathbb{c}_0^{-1} : \mathbb{c}_r - \mathbb{I})]^{-1} \right\}$ and $[\square] = [\mathbb{I} + \mathbb{S}_i : (\mathbb{c}_0^{-1} : \mathbb{c}_i - \mathbb{I})]$.

material tensor

$$\begin{aligned}\mathbb{C}_{eff} &= f_0\mathbb{c}_0 : \langle \mathbb{A}(\mathbf{x})\rangle_{V_0} + f_i\mathbb{c}_i : \mathbb{A}_i \\ &= \left\{\sum_{r\in 0,i} f_r\mathbb{c}_r : \left[\mathbb{I} + \mathbb{S}_r : (\mathbb{c}_0^{-1} : \mathbb{c}_r - \mathbb{I})\right]^{-1}\right\} \\ &\quad : \left\{\sum_{r\in 0,i} f_r \left[\mathbb{I} + \mathbb{S}_r : (\mathbb{c}_0^{-1} : \mathbb{c}_r - \mathbb{I})\right]^{-1}\right\}^{-1} . \end{aligned} \tag{B.11}$$

Equation (B.11) can be extended to multiple types of inclusions, reading

$$\mathbb{C}_{eff} = \left\{\sum_{r} f_r\mathbb{c}_r : \left[\mathbb{I} + \mathbb{S}_r : (\mathbb{c}_0^{-1} : \mathbb{c}_r - \mathbb{I})\right]^{-1}\right\} : \left\{\sum_{r} f_r \left[\mathbb{I} + \mathbb{S}_r : (\mathbb{c}_0^{-1} : \mathbb{c}_r - \mathbb{I})\right]^{-1}\right\}^{-1} , \tag{B.12}$$

with $r \in$ { matrix material = reference medium 0, inclusion 1, inclusion 2, ... } for the case of the MT scheme. In the following, Equation (B.12) is specialized for the application to cement-based materials, characterized by isotropic material behavior. Thus, Equation (B.12) can be reduced to the specification of the effective shear and bulk modulus, μ_{eff} and k_{eff}, respectively:

$$\mu_{eff} = \frac{\sum_r f_r\mu_r \left[1 + \beta\left(\frac{\mu_r}{\mu_m} - 1\right)\right]^{-1}}{\sum_r f_r \left[1 + \beta\left(\frac{\mu_r}{\mu_m} - 1\right)\right]^{-1}} \quad \text{and} \quad k_{eff} = \frac{\sum_r f_r k_r \left[1 + \alpha\left(\frac{k_r}{k_m} - 1\right)\right]^{-1}}{\sum_r f_r \left[1 + \alpha\left(\frac{k_r}{k_m} - 1\right)\right]^{-1}} , \tag{B.13}$$

where α and β represent the volumetric and deviatoric part of the Eshelby tensor $\mathbb{S}$ specialized for spherical inclusions, reading

$$\alpha = \frac{3k_m}{3k_m + 4\mu_m} \quad \text{and} \quad \beta = \frac{6(k_m + 2\mu_m)}{5(3k_m + 4\mu_m)} . \tag{B.14}$$

B.2 Upscaling of creep properties

Viscous material response is characterized by (i) an increase of deformation during constant loading (creep) and (ii) a decrease of stress for constraint deformation (relaxation). The viscous response is commonly described by the creep compliance J [Pa^{-1}] and the relaxation modulus R [Pa], both dependent on time. The creep compliance associated with uniaxial loading is determined as

$$J(t) = \frac{\varepsilon(t)}{\sigma_0}, \tag{B.15}$$

with $\varepsilon(t)$ denoting the measured strain, and σ_0 representing the applied constant stress. The relaxation modulus, on the other hand, is determined from the measured stress decrease $\sigma(t)$ in consequence of a constant strain ε_0 as

$$R(t) = \frac{\sigma(t)}{\varepsilon_0}. \tag{B.16}$$

Introducing the Boltzmann convolution integral, Equations (B.15) and (B.16) can be expanded towards variable (non-constant) stress or strain histories, respectively:

$$\varepsilon(t) = \int_0^t J(t-\tau)\frac{\partial\sigma(\tau)}{\partial\tau}d\tau \quad \text{and} \quad \sigma(t) = \int_0^t R(t-\tau)\frac{\partial\varepsilon(\tau)}{\partial\tau}d\tau \ , \tag{B.17}$$

where τ denotes the time instant of loading. Applying the Laplace transform[3] to Equations (B.17) gives

$$\hat{\varepsilon}(p) = p\hat{J}(p)\hat{\sigma}(p) \quad \text{and} \quad \hat{\sigma}(p) = p\hat{R}(p)\hat{\varepsilon}(p) \ , \quad \text{with} \quad p\hat{J}(p) = \frac{1}{p\hat{R}(p)} \ , \tag{B.21}$$

considering that the Laplace transform of the convolution integral becomes a multiplication and $\partial\varepsilon/\partial\tau$ turns into $p\hat{\varepsilon}$. Considering the definition of the Laplace-Carson transformation as $f^\star = p\hat{f}$ in Equations (B.21) yields

$$\varepsilon^\star(p) = J^\star(p)\sigma^\star(p) \quad \text{and} \quad \sigma^\star(p) = R^\star(p)\varepsilon^\star(p) \ , \quad \text{with} \quad J^\star(p) = \frac{1}{R^\star(p)} \ . \tag{B.22}$$

The analogous form of $\sigma^\star = R^\star\varepsilon$ in Equation (B.22) and the elastic constitutive law $\sigma = E\varepsilon$ is the basis for the "correspondence principle" [13, 11]. According to this principle, viscoelastic problems can be solved using the respective solution of the elastic problem in the Laplace-Carson domain. Hereby, elastic material parameters, e.g., the shear compliance $J^{dev} = 1/\mu$, where μ is the shear modulus, are replaced by the Laplace-Carson transform of the respective viscoelastic material parameters, e.g., the Laplace-Carson transform of the

[3]Whereas the Laplace transformation of $f(t)$ is defined as

$$\mathcal{L}[f(t)] = \hat{f}(p) = \int_0^\infty f(t)e^{-pt}dt, \tag{B.18}$$

with p as the complex variable. The Laplace-Carson transformation of $f(t)$ is given as

$$\mathcal{LC}[f(t)] = f^\star(p) = p\int_0^\infty f(t)e^{-pt}dt. \tag{B.19}$$

Hence, $f^\star(p) = p\hat{f}(p)$. The inverse Laplace-Carson transformation is defined in the complex plane as

$$\mathcal{LC}^{-1}[f^\star(p)] = f(t) = \frac{1}{2i\pi}\int_\Omega \frac{f^\star(p)}{p}e^{pt}dp, \tag{B.20}$$

where Ω is a parallel to the imaginary axis having all poles of $f^\star(p)$ to the left.

creep compliance associated with deviatoric creep $J^{dev\star}$. The solution of the viscoelastic problem in the time domain is obtained by inverse Laplace-Carson transformation. E.g., application of the correspondence principle to the MT scheme introduced for upscaling of elastic properties in Subsection B.1 gives access to the effective creep compliance of matrix-inclusion type composites (see, e.g., [3] for the application of the correspondence principle to the self-consistent scheme).

Appendix C

Eshelby tensor for cylindrical inclusions

The Eshelby tensor for the case of cylindrical inclusions for the plane-strain situation is given by [7]:

$$\mathbb{S}_a = \begin{pmatrix} \frac{-5+4\nu_m}{8(\nu_m-1)} & -\frac{4\nu_m-1}{8(\nu_m-1)} & \frac{\nu_m}{2(1-\nu_m)} & 0 & 0 & 0 \\ -\frac{4\nu_m-1}{8(\nu_m-1)} & \frac{-5+4\nu_m}{8(\nu_m-1)} & \frac{\nu_m}{2(1-\nu_m)} & 0 & 0 & 0 \\ 0 & 0 & 0 & 0 & 0 & 0 \\ 0 & 0 & 0 & \frac{-3+4\nu_m}{8(\nu_m-1)} & 0 & 0 \\ 0 & 0 & 0 & 0 & \frac{1}{4} & 0 \\ 0 & 0 & 0 & 0 & 0 & \frac{1}{4} \end{pmatrix}, \qquad \text{(C.1)}$$

where ν_m is Poisson's ratio of the matrix material.

Appendix D

Hooke's law for transversal isotropic materials

$$\begin{Bmatrix} \varepsilon_{xx} \\ \varepsilon_{yy} \\ \varepsilon_{zz} \\ 2\varepsilon_{xy} \\ 2\varepsilon_{xz} \\ 2\varepsilon_{zx} \end{Bmatrix} = \underbrace{\begin{bmatrix} \frac{1}{E_{x,y}} & -\frac{\nu_{xy}}{E_{x,y}} & -\frac{\nu_{(x,y)z}}{E_z} & 0 & 0 & 0 \\ -\frac{\nu_{xy}}{E_{x,y}} & \frac{1}{E_{x,y}} & -\frac{\nu_{(x,y,z}}{E_z} & 0 & 0 & 0 \\ -\frac{\nu_{(x,y)z}}{E_z} & -\frac{\nu_{(x,y)z}}{E_z} & \frac{1}{E_z} & 0 & 0 & 0 \\ 0 & 0 & 0 & \frac{2(1+\nu_{xy})}{E_{x,y}} & 0 & 0 \\ 0 & 0 & 0 & 0 & \frac{1}{\mu_{(x,y)z}} & 0 \\ 0 & 0 & 0 & 0 & 0 & \frac{1}{\mu_{(x,y)z}} \end{bmatrix}}_{\text{compliance tensor } \mathbb{D} = \mathbb{C}^{-1}} \begin{Bmatrix} \sigma_{xx} \\ \sigma_{yy} \\ \sigma_{zz} \\ \sigma_{xy} \\ \sigma_{xz} \\ \sigma_{zx} \end{Bmatrix} \tag{D.1}$$

Appendix E

FE meshes representing matrix-inclusion materials used in Subsection 2.1

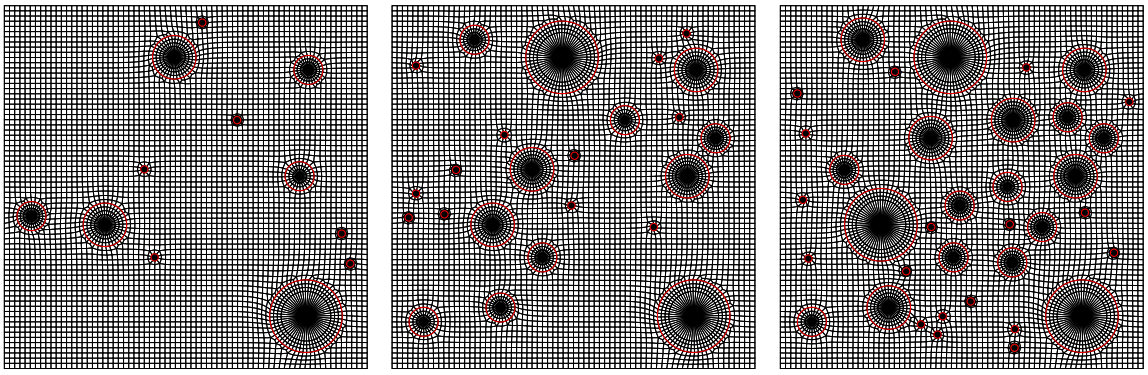

f_a=0.071 f_a=0.142 f_a=0.213

Figure E.1: FE meshes: $f_a \leq 0.25$

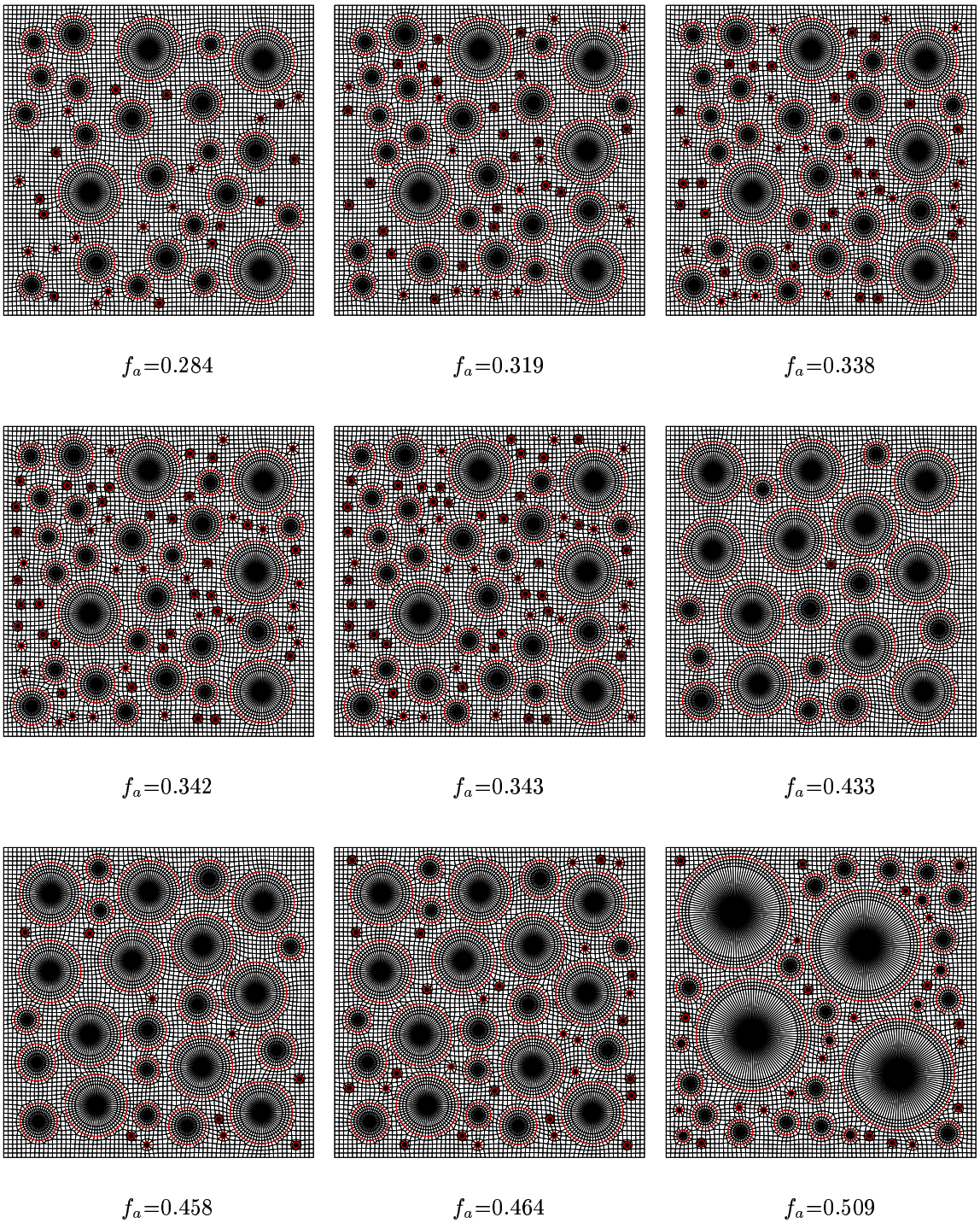

f_a=0.284 f_a=0.319 f_a=0.338

f_a=0.342 f_a=0.343 f_a=0.433

f_a=0.458 f_a=0.464 f_a=0.509

Figure E.2: FE meshes: $0.25 \leq f_a \leq 0.55$

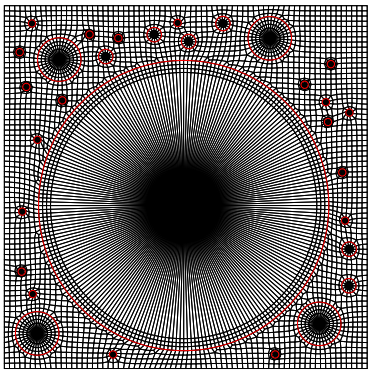

f_a=0.562

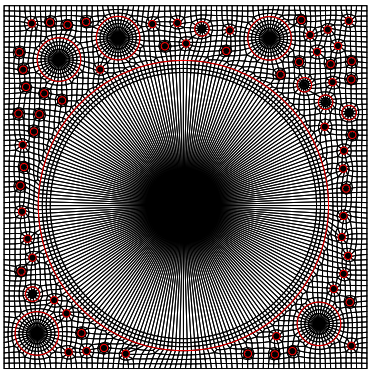

f_a=0.585

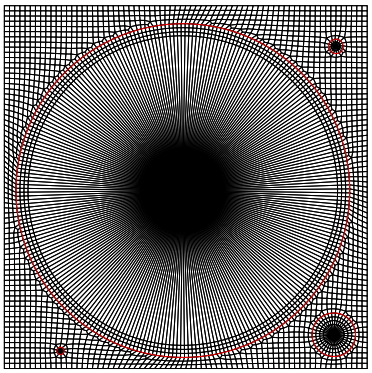

f_a=0.678

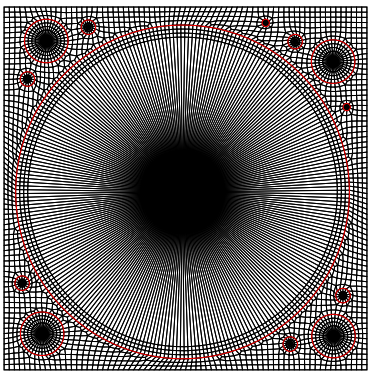

f_a=0.718

Figure E.3: FE meshes: $0.55 \leq f_a$

Appendix F

Effective creep compliances for the case of cylindrical inclusions

F.1 J_{eff}^{dev} and J_{eff}^{vol} for Maxwell model

Applying the correspondence principle to the effective creep compliance obtained by the MT scheme [Equation (2.6)], the Laplace-Carson transform of the effective deviatoric creep compliance reads:

$$J_{eff}^{dev\star}(p) = \frac{1}{\mu_{eff}^{\star}(p)} = \frac{1}{\mu_m^{\star} + f_a \dfrac{\mu_a^{\star} - \mu_m^{\star}}{1 + (1-f_a)\dfrac{\mu_a^{\star} - \mu_m^{\star}}{2\mu_m^{\star}\dfrac{k_m^{\star} + \mu_m^{\star}}{k_m^{\star} + 2\mu_m^{\star}}}}} =$$

$$= \frac{1}{\dfrac{\eta\mu_m p}{\mu_m + \eta p} + \dfrac{f_a(\mu_a - \dfrac{\eta\mu_m p}{\mu_m + \eta p})}{\dfrac{(1-f_a)(\mu_m + \eta p)(\mu_a - \dfrac{\eta\mu_m p}{\mu_m + \eta p})(k_m + \dfrac{2\eta\mu_m p}{\mu_m + \eta p})}{2\eta\mu_m p(k_m + \dfrac{\eta\mu_m p}{\mu_m + \eta p})} + 1}}, \tag{F.1}$$

where the Laplace-Carson transform of the deviatoric creep compliance of the matrix material is given for the Maxwell model as:

$$J_m^{dev\star}(p) = \frac{1}{\mu_m^{\star}(p)} = \mathcal{LC}\left[J_m^{dev}(t)\right] = \frac{1}{\mu_m} + \frac{1}{\eta p} \quad \rightarrow \quad \mu_m^{\star}(p) = \frac{\mu_m \eta p}{\eta p + \mu_m}. \tag{F.2}$$

Assuming (i) the cylindrical particles to exhibit elastic behavior, with $\mu_a^{\star} = \mu_a$, and (ii) the matrix material to exhibit elastic behavior under hydrostatic loading, $k_m^{\star} = k_m$, the inverse Laplace-Carson transformation [see Equation (B.20)] gives access to the effective

deviatoric creep compliance in the time domain:

$$J_{eff}^{dev}(t) = \mathcal{LC}^{-1}\left[J_{eff}^{dev\star}(p)\right] = \frac{N}{D}, \tag{F.3}$$

with

$$\begin{aligned} N = {} & \eta(-\mu_a(\mu_a-\mu_m)k_m(2\mu_m+k_m){f_a}^3 \\ & + (((-4+4\bullet){\mu_m}^2 - 2k_m\mu_m - {k_m}^2){\mu_a}^2 + \mu_m k_m((-4+8\bullet)\mu_m + 3k_m)\mu_a \\ & + 4(-1+\bullet){\mu_m}^2{k_m}^2){f_a}^2 + (((4-4\bullet){\mu_m}^2 + 2k_m\mu_m + {k_m}^2){\mu_a}^2 \\ & + \mu_m k_m((10-8\bullet)\mu_m + 3k_m)\mu_a + 4(1-\bullet){\mu_m}^2{k_m}^2)f_a \\ & + \mu_a k_m(\mu_m k_m + \mu_a(2\mu_m + k_m))) \\ & - ({f_a}^2 - 1)\mu_a\mu_m k_m(\mu_a(2\mu_m + f_a k_m + k_m) - (f_a-1)\mu_m k_m)t \end{aligned} \tag{F.4}$$

$$\bullet = \exp\left[-\frac{(f_a+1)\mu_a\mu_m k_m t}{\eta(\mu_a(2\mu_m + f_a k_m + k_m) - (f_a-1)\mu_m k_m)}\right] \tag{F.5}$$

and

$$D = \eta(f_a+1)^2\mu_a\mu_m k_m\left[\mu_a(2\mu_m + f_a k_m + k_m) - (f_a-1)\mu_m k_m\right]. \tag{F.6}$$

In analogy to Equation (F.1), the Laplace-Carson transform of the effective volumetric creep compliance is obtained from Equation (2.7) as:

$$J_{eff}^{vol\star}(p) = \frac{1}{k_{eff}^{\star}(p)} = \frac{1}{k_m^{\star} + f_a\dfrac{k_a^{\star}-k_m^{\star}}{1+(1-f_a)\dfrac{k_a^{\star}-k_m^{\star}}{k_m^{\star}+\mu_m^{\star}}}} = \frac{1}{\dfrac{f_a(k_a-k_m)}{\dfrac{(1-f_a)(k_a-k_m)}{k_m + \dfrac{\eta\mu_m p}{\mu_m+\eta p}} + 1} + k_m}. \tag{F.7}$$

Performing the inverse Laplace-Carson transformation gives access to the effective volumetric creep compliance:

$$\begin{aligned} J_{eff}^{vol}(t) &= \mathcal{LC}^{-1}\left[J_{eff}^{vol\star}(p)\right] = \\ &= \frac{\exp\left[-\dfrac{\mu_m k_a k_m t}{\eta(f_a\mu_m(k_a-k_m) + (\mu_m+k_a)k_m)}\right](f_a-1)f_a\mu_m(k_a-k_m)^2}{f_a\mu_m(k_a-k_m) + (\mu_m+k_a)k_m} - f_a k_a + k_a + f_a k_m \\ &\qquad\qquad k_a k_m \end{aligned} \tag{F.8}$$

In case of cylindrical pores, the effective creep compliances are obtained from Equations

(2.9) and (2.10):

$$J_{eff}^{dev\star}(p) = \frac{1}{\mu_{eff}^{\star}(p)} = \frac{1}{\mu_m^{\star} - \dfrac{f_p \mu_m^{\star}}{1 - \dfrac{(1-f_p)(\eta p + \mu_m^{\star})(k_m + 2\mu_m^{\star})}{2\eta p (k_m^{\star} + \mu_m^{\star})}}}$$

$$= \frac{1}{\dfrac{\eta \mu_m p}{\mu_m + \eta p} - \dfrac{\eta f_p \mu_m p}{(\mu_m + \eta p)\left(1 - \dfrac{(1-f_p)\left(k_m + \dfrac{2\eta\mu_m p}{\mu_m + \eta p}\right)}{2\left(k_m + \dfrac{\eta \mu_m p}{\mu_m + \eta p}\right)}\right)}} \tag{F.9}$$

$$J_{eff}^{dev}(t) = \mathcal{LC}^{-1}\left[J_{eff}^{dev\star}(p)\right] = \frac{2\eta f_p \mu_m + f_p k_m t \mu_m + k_m t \mu_m + \eta k_m + \eta f_p k_m}{\eta \mu_m k_m - \eta f_p \mu_m k_m} \tag{F.10}$$

and

$$J_{eff}^{vol\star}(p) = \frac{1}{k_{eff}^{\star}(p)} = \frac{1}{k_m^{\star} - \dfrac{f_p k_m^{\star}}{1 - \dfrac{(1-f_p)k_m^{\star}}{k_m^{\star} + \mu_m^{\star}}}} = \frac{1}{k_m - \dfrac{f_p k_m}{1 - \dfrac{(1-f_p)k_m}{k_m + \dfrac{\eta \mu_m p}{\mu_m + \eta p}}}} \tag{F.11}$$

$$J_{eff}^{vol}(t) = \mathcal{LC}^{-1}\left[J_{eff}^{vol\star}(p)\right] = \frac{\eta \mu_m + f_a k_m t \mu_m + \eta f_a k_m}{\eta \mu_m k_m - \eta f_a \mu_m k_m}. \tag{F.12}$$

F.2 J_{eff}^{dev} and J_{eff}^{vol} for three-parameter model

For the three-parameter model, the Laplace-Carson transform of the deviatoric creep compliance of the matrix material reads

$$J_m^{dev\star}(p) = \frac{1}{\mu_m^{\star}(p)} = \mathcal{LC}\left[J_m^{dev}(t)\right] = \frac{1}{\mu_m} + \frac{1}{\mu_v + \eta p} \qquad \mu_m^{\star}(p) = \frac{\mu_m(\mu_v + \eta p)}{\mu_m + \mu_v + \eta p} \tag{F.13}$$

giving the Laplace-Carson transform of the effective deviatoric creep compliance as

$$J_{eff}^{dev\star}(p) = \frac{1}{\mu_{eff}^{\star}(p)} = \frac{1}{\mu_m^{\star} + f_a \dfrac{\mu_a^{\star} - \mu_m^{\star}}{1 + (1-f_a)\dfrac{\mu_a^{\star} - \mu_m^{\star}}{2\mu_m^{\star}\dfrac{k_m^{\star} + \mu_m^{\star}}{k_m^{\star} + 2\mu_m^{\star}}}}} =$$

$$= \frac{1}{\dfrac{\mu_m(\mu_v + \eta p)}{\mu_m + \mu_v + \eta p} + \dfrac{f_a\left(\mu_a - \frac{\mu_m(\mu_v+\eta p)}{\mu_m+\mu_v+\eta p}\right)}{\frac{(1-f_a)(\mu_m+\mu_v+\eta p)\left(\mu_a - \frac{\mu_m(\mu_v+\eta p)}{\mu_m+\mu_v+\eta p}\right)\left(k_m + \frac{2\mu_m(\mu_v+\eta p)}{\mu_m+\mu_v+\eta p}\right)}{2\mu_m(\mu_v+\eta p)\left(k_m + \frac{\mu_m(\mu_v+\eta p)}{\mu_m+\mu_v+\eta p}\right)} + 1}}. \tag{F.14}$$

Application of the inverse Laplace-Carson transformation to Equation (F.14) gives

$$
\begin{aligned}
J_{eff}^{dev}(t) &= \mathcal{LC}^{-1}\left[J_{eff}^{dev\star}(p)\right] = \\
&\frac{4e^{-\frac{\diamond t}{\eta(\mu_a(2\mu_m+f_ak_m+k_m)-(f_a-1)\mu_mk_m)}}(f_a-1)f_a\mu_m^2(\mu_a+k_m)^2}{(f_a+1)(\mu_a(2\mu_m+f_ak_m+k_m)-(f_a-1)\mu_mk_m)\diamond} \\
&+\frac{\mu_m\mu_v((\mu_m+\mu_v)k_m+f_a(\mu_vk_m+\mu_m(2\mu_v+k_m)))}{\mu_m\mu_v(\mu_a((f_a+1)\mu_vk_m+\mu_m(2\mu_v+f_ak_m+k_m))-(f_a-1)\mu_m\mu_vk_m)} \\
&-\frac{(f_a-1)\mu_a(\mu_m+\mu_v)(\mu_vk_m+\mu_m(2\mu_v+k_m))}{\mu_m\mu_v(\mu_a((f_a+1)\mu_vk_m+\mu_m(2\mu_v+f_ak_m+k_m))-(f_a-1)\mu_m\mu_vk_m)} \\
&+\frac{\exp\left[-\frac{\mu_vt}{\eta}\right](f_a-1)}{(f_a+1)\mu_v}
\end{aligned}
\tag{F.15}
$$

with

$$
\diamond = \mu_a\left[(f_a+1)\mu_vk_m+\mu_m(2\mu_v+f_ak_m+k_m)\right]-(f_a-1)\mu_m\mu_vk_m. \tag{F.16}
$$

In a similar manner, the Laplace-Carson transform of the effective volumetric creep compliance is obtained as

$$
J_{eff}^{vol\star}(p) = \frac{1}{k_{eff}^{\star}(p)} = \frac{1}{k_m^{\star}+f_a\frac{k_a^{\star}-k_m^{\star}}{1+(1-f_a)\frac{k_a^{\star}-k_m^{\star}}{k_m^{\star}+\mu_m^{\star}}}} = \frac{1}{\frac{f_a(k_a-k_m)}{\frac{(1-f_a)(k_a-k_m)}{k_m+\frac{\mu_m(\mu_v+\eta p)}{\mu_m+\mu_v+\eta p}}+1}+k_m}. \tag{F.17}
$$

Application of the inverse Laplace-Carson transformation gives

$$
\begin{aligned}
J_{eff}^{vol}(t) &= \mathcal{LC}^{-1}\left[J_{eff}^{vol\star}(p)\right] = \\
&= \frac{\bullet(\mu_m-f_ak_a+k_a+f_ak_m)}{f_a\mu_m(k_a-k_m)+(\mu_m+k_a)k_m} \\
&-\frac{\bullet(\mu_v(-f_ak_a+k_a+f_ak_m)+\mu_m(\mu_v-f_ak_a+k_a+f_ak_m))}{f_a\mu_m\mu_v(k_a-k_m)+(\mu_vk_a+\mu_m(\mu_v+k_a))k_m} \\
&+\frac{\mu_v(-f_ak_a+k_a+f_ak_m)+\mu_m(\mu_v-f_ak_a+k_a+f_ak_m)}{f_a\mu_m\mu_v(k_a-k_m)+(\mu_vk_a+\mu_m(\mu_v+k_a))k_m},
\end{aligned}
\tag{F.18}
$$

with

$$
\bullet = \exp\left[-\frac{(f_a\mu_m\mu_v(k_a-k_m)+(\mu_vk_a+\mu_m(\mu_v+k_a))k_m)t}{\eta(f_a\mu_m(k_a-k_m)+(\mu_m+k_a)k_m)}\right]. \tag{F.19}
$$

In case of cylindrical pores, the effective deviatoric and volumetric creep-compliance functions are obtained as:

$$J_{eff}^{dev\star}(p) = \frac{1}{\mu_{eff}^{\star}(p)} = \frac{1}{\mu_m^{\star} - \dfrac{f_p \mu_m^{\star}}{1 - \dfrac{(1-f_p)(\eta p + \mu_m^{\star})(k_m + 2\mu_m^{\star})}{2\eta p (k_m^{\star} + \mu_m^{\star})}}} =$$

$$= \frac{1}{\dfrac{\mu_m(\mu_v + \eta p)}{\mu_m + \mu_v + \eta p} - \dfrac{f_a \mu_m (\mu_v + \eta p)}{(\mu_m + \mu_v + \eta p)\left(1 - \dfrac{(1-f_a)\left(k_m + \dfrac{2\mu_m(\mu_v + \eta p)}{\mu_m + \mu_v + \eta p}\right)}{2\left(k_m + \dfrac{\mu_m(\mu_v + \eta p)}{\mu_m + \mu_v + \eta p}\right)}\right)}} \tag{F.20}$$

$$J_{eff}^{dev}(t) = \mathcal{LC}^{-1}\left[J_{eff}^{dev\star}(p)\right] =$$

$$= \frac{2 f_a \mu_m \mu_v + f_a k_m \mu_v + k_m \mu_v + (1 - exp\left[-\dfrac{\mu_v t}{\eta}\right])\mu_m k_m + (1 - exp\left[-\dfrac{\mu_v t}{\eta}\right]) f_a \mu_m k_m}{\mu_m \mu_v k_m - f_a \mu_m \mu_v k_m} \tag{F.21}$$

and

$$J_{eff}^{vol\star}(p) = \frac{1}{k_{eff}^{\star}(p)} = \frac{1}{k_m^{\star} - \dfrac{f_p k_m^{\star}}{1 - \dfrac{(1-f_p)k_m^{\star}}{k_m^{\star} + \mu_m^{\star}}}} = \frac{1}{k_m - \dfrac{f_a k_m}{1 - \dfrac{(1-f_a)k_m}{k_m + \dfrac{\mu_m(\mu_v + \eta p)}{\mu_m + \mu_v + \eta p}}}} \tag{F.22}$$

$$J_{eff}^{vol}(t) = \mathcal{LC}^{-1}\left[J_{eff}^{vol\star}(p)\right] = \frac{\mu_m \mu_v + f_a k_m \mu_v - exp\left[-\frac{\mu_v t}{\eta}\right] f_a \mu_m k_m + f_a \mu_m k_m}{\mu_m \mu_v k_m - f_a \mu_m \mu_v k_m}. \tag{F.23}$$

Appendix G

Recipes for the tested types of shotcrete

Lainzer Tunnel LT31	
CEM I 52.5 R, Lafarge, Mannersdorf	378 kg/m^3
Fluamix C, company Lafarge, plant Mannersdorf	43 kg/m^3
aggregate RK 0/4, Reiterer	872 kg/m^3
aggregate RK 0/4, Springer	432 kg/m^3
aggregate RK 4/8, Reiterer	412 kg/m^3
total water	209 kg/m^3
superplasticizer ECO-SL 2,5-5,0 (Betontechnik)	4.6 kg/m^3
accelerating admixture *Mapequick*	6.5 m-% of (cement+Fluamix)
total mass	2375 kg/m^3

Lainzer Tunnel LT33	
CEM II 42.5 R, Lafarge, Mannersdorf	430 kg/m^3
aggregate RK 0/4	1176 kg/m^3
aggregate RK 4/8	504 kg/m^3
total water	190 kg/m^3
superplasticizer	0.9 m-% of cement
air-entraining agent	0.02 m-% of cement
accelerating admixture	0.75 m-% of cement
total mass	2307 kg/m^3

Lainzer Tunnel LT44	
CEM II A/M 42.5 N, Lafarge, Mannersdorf	350 kg/m^3
total water	193 kg/m^3
aggregate (lime, dolomite)	1840 kg/m^3
total mass	2383 kg/m^3